РОССИЙСКИЙ ГОСУДАРСТВЕННЫЙ ПЕДАГОГИЧЕСКИЙ УНИВЕРСИТЕТ им. А. И. ГЕРЦЕНА
HERZEN STATE PEDAGOGICAL UNIVERSITY of RUSSIA

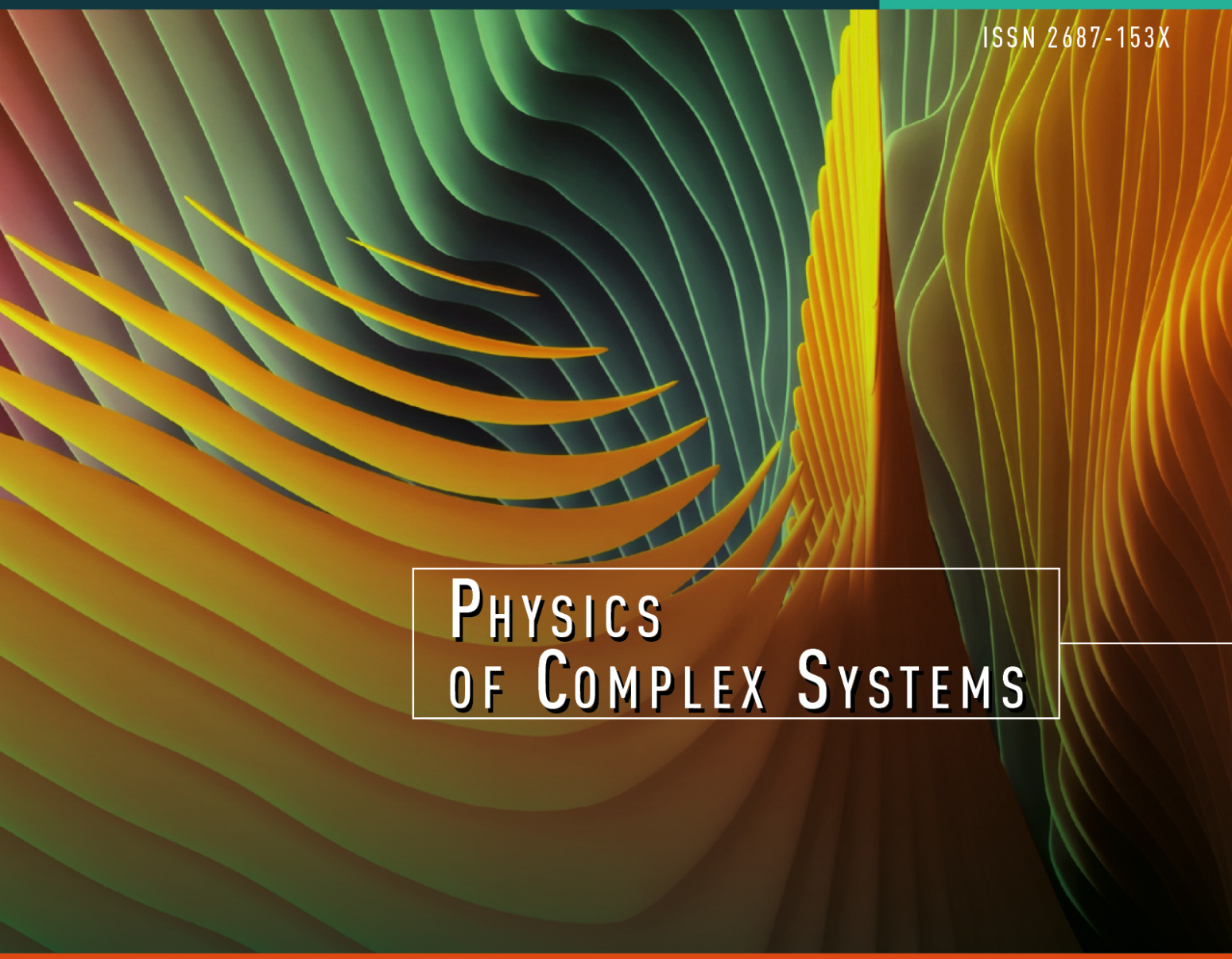

ISSN 2687-153X

Physics of Complex Systems

Т. 2 № 4 2021

Vol. 2 No. 4 2021

Herzen State Pedagogical University of Russia

ISSN 2687-153X (online)
physcomsys.ru
https://www.doi.org/10.33910/2687-153X-2021-2-4
2021. Vol. 2, no. 4

PHYSICS OF COMPLEX SYSTEMS

Mass Media Registration Certificate El No. FS77-77889, issued by Roskomnadzor on 10 February 2020
Peer-reviewed journal
Open Access
Published since 2020
4 issues per year

Publishing house of Herzen State Pedagogical University of Russia
48 Moika Emb., Saint Petersburg 191186, Russia
E-mail: izdat@herzen.spb.ru
Phone: +7 (812) 312-17-41

Data size 4,31 Mbyte
Published at 29.12.2021

Editors of the English text *I. A. Nagovitsyna, A. S. Samarsky*
Cover design by *O. V. Rudneva*
Layout by *A. M. Khodan, L. N. Kliuchanskaya*

CONTENTS

Condensed Matter Physics **141**

Belo A. F., Shimakawa K. Statistical and spectral analysis of wind power: ractional oscillation dynamics 141

Gorokhovatskiy Yu. A., Karulina E. A., Ignatyeva D. A. Nature and mechanisms of relaxation processes in biocompatible polylactide films 149

Shabanova N. S., Temnov D. E. Analysis of the TSD spectra of polymers near the glass transition temperature using the fractional purification method 157

Physics of Semiconductors **165**

Nemov S. A., Andreeva V. D., Volkhin V., Proklova V. Yu., Ulashkevich Yu. V. The valence zone structure in $PbSb_2Te_4$ and anisotropy of hole relaxation time 165

Semenov A. R., Kholomina T. A., Litvinov V. G., Ermachikhin A. V. Investigation of the properties of zinc oxide based heterostructures 172

Theoretical physics **180**

Grib A. A., Vertogradov V. D., Shleiger L. A. Forces for the particles with a zero energy in Kerr metric 180

Condensed Matter Physics.
General Relativity and Gravity

UDC 551.46; 53.09 https://www.doi.org/10.33910/2687-153X-2021-2-4-141-148

Statistical and spectral analysis of wind power: Fractional oscillation dynamics

A. F. Belo✉[1], K. Shimakawa[2]

[1] East Timor National University, Av. Cidade de Lisboa, Díli, East Timor
[2] Gifu University, 1–1 Yanagido, Gifu 501-1193, Japan

Authors
Abelito F. Belo, e-mail: abelitofilipe@gmail.com
Koichi Shimakawa, e-mail: koichi@gifu-u.ac.jp

For citation: Belo, A. F., Shimakawa, K. (2021) Statistical and spectral analysis of wind power: Fractional oscillation dynamics. *Physics of Complex Systems*, 2 (4), 141–148. https://www.doi.org/10.33910/2687-153X-2021-2-4-141-148
Received 3 September 2021; reviewed 22 September 2021; accepted 22 September 2021.
Funding: This work has been performed within JICA-CADEFEST 2 project.

Abstract. Time-dependent changes of the wind speed, as for example in Hera Campus (East Timor), are analysed by the statistical and the autocorrelation function in time domain and by the frequency spectrum (frequency domain) using the Fast Fourier Transform (FFT). The wind speed can be modelled using the Weibull distribution function. The autocorrelation function in time domain shows roughly a non-exponential decay with periodicity. The power spectrum shows two peaks and nearly $1/f^{\alpha}$ nature at high frequencies, close to the Kolmogorov prediction with $\alpha = 5/3$. A Cole-Davidson type generalisation of wind dynamics, originating from the fractional dynamics of oscillation, is different from the dynamics of tides.

Keywords: wind power, statistical analysis, Weibull probability distribution, autocorrelation function, Kolmogorov spectrum.

Introduction

Wind power should be one of the major inputs for producing sustainable environmental conditions of globe (Hasche 2010; Joselin Herbert et al. 2007). Worldwide wind power generation is now increasing significantly. Wind turbines are often used in large-scale wind farms in the countryside or in coastal regions. However, there has been a growing market for small-scale local farms with large numbers, evolving commercially helpful (Murthy, Rahi 2014; Norheim, Pudjianto 2008).

Wind power, however, is not stable, and the power produced by turbines varies with time. We should know the characteristic feature of variations in the local wind farms, because the nature of wind depends highly on locations. There are several ways to analyse wind characters in time and/or frequency domain. In the time domain, one simple way is to construct statistically a histogram of the step size (wind speed etc.) in output over time (Murthy, Rahi 2014; Wan, Bucaneg 2002). To understand the nature of *wind quality*, introducing the autocorrelation function (AF) can be useful. The other is to elucidate frequency spectrum (FS) (power spectrum) in frequency domain, which is helpful to understand the nature of wind power in details. From the AF and FS, it is easy to know randomness and periodicity of the wind power (Apt 2007).

In the present paper, as a series report of the tide dynamics (Belo et al. 2021), by using a small-size wind generator, we elucidate the nature of wind power at the Hera campus, Universidade Nacional Timor Lorosa'e, East Timor (8.55° S, 125.56° E). The wind speed variations throughout three months (June to September 2019) will be characterised in terms of a histogram, a probability distribution, and a power spectrum through the Fast Fourier Transform (FFT). The power spectrum shows two peaks (half and full days) with the high frequency tail of $1/f^{\alpha}$. The a-value closes to 5/3, which is known to be the Kolmogorov parameter found in turbulence (Apt 2007). It is discussed that the physical origin of the parameter a lies in the fractional dynamics of wind power, which leads to the Cole-Davidson type relaxation (Nigmatullin, Ryabov 1997). This is different from the dynamics of tide (Belo et al. 2021), in which a Lorentz-type relaxation is found in the frequency domain.

The autocorrelation function will be also elucidated from the time variation of wind speed, showing how much randomness is involved in the examined wind power (Belu, Koracin 2013). It is shown that the correlation time (memory effect of wind) is around 6 h, which may be related to the duration of Kolmogorov's turbulence.

Experimental and analytical technique

The data analysed in this work were collected between June 2019 and September 2019. Fig. 1 shows the 600-watt wind generator set (Nantong R&X Energy Technology: RX — 600H3) at Hera campus located 10 km east of Dili city.

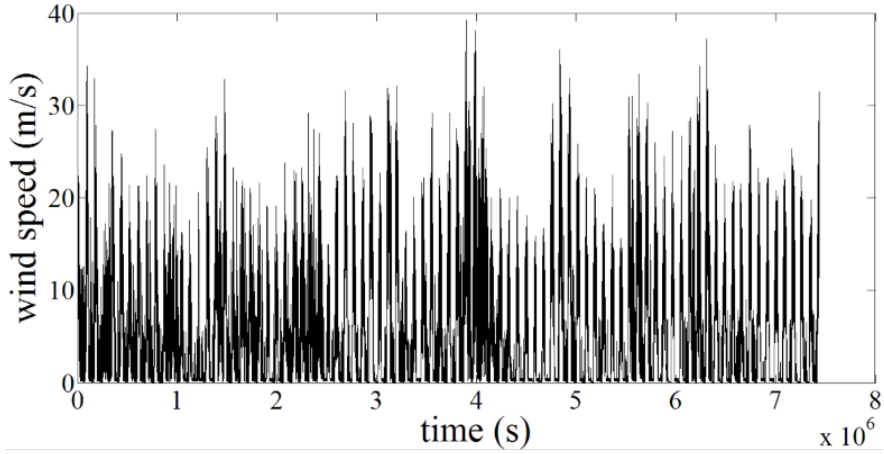

Fig. 1. Time-variation of the wind speed $v(t)$ at every 100 seconds for three months (8×10^6 s) at Hera campus (June to September 2019)

Wind speed was measured at the 6 m tall instrumented towers. The output voltage of wind turbine was transferred to the Data Logger (DL) (Belo et al. 2020). Data of the wind speed at every 100 seconds were stored in the PC. Collected data with the DL were Fourier transformed (Fast Fourier Transform: FFT). Fourier analysis converts a signal from its original time domain to the frequency domain. The FT of a time-dependent function $v(t)$ is given by

$$v(f) = \int_{-\infty}^{\infty} v(t) e^{-i2\pi ft} dt, \tag{1}$$

where $v(f)$ is the Fourier spectrum and f the frequency (s^{-1}) (Papoulis 1962). The FFT is an algorithm that computes the discrete $v(f)$ (Zonst 2004). Data of the wind speed at every 100 seconds for 3 months (data number N = 74398) are Fourier transformed using the MATLAB.

Elucidation of the autocorrelation function C(t) obtained, on the other hand, from the raw data is defined as

$$C(\tau) = \langle v(t) v(t+\tau) \rangle, \tag{2}$$

where < > is the time average, τ is called the correlation time. Note here that variation $v(t)$ is given as $v(t) = v'(t) - \langle v'(t) \rangle$, where $v'(t)$ is the raw data, giving therefore $\langle v(t) \rangle = 0$. When $\tau = 0$, $C(\tau) = C(0) = \langle v(t) v(t) \rangle = \langle v(t)^2 \rangle$, where $\langle v(t)^2 \rangle$ is called the *variance*.

 https://www.doi.org/10.33910/2687-153X-2021-2-4-141-148

$C(\tau) = 0$ means no correlation, i. e., no memory on a previous event after a time τ. The autocorrelation therefore shows to what extent the event in future is related to the past.

Results and discussion

Fig. 1 shows the measured time-dependent wind speed $v(t)$ at every 100 seconds for three months (8×10^6 s) at Hera campus (June to September 2019). The maximum wind speed is 35 m/s and the minimum is 0 m/s, with roughly 1-day periodicity (diurnal) and its second harmonics, which is a general trend in wind power reported in other areas (Apt 2007).

Fig. 2 shows the histogram for the wind speed $v(t)$ in which the probability density at a particular wind speed is obtained. The number of occurrences of each speed is counted for this object. Discrete bars shown in Fig. 2 present the wind speed distribution for the total number of data ($N_T = 74398$). It is known that the Weibull distribution is well-accepted and widely used for wind data analysis (Matsfelt, Davidson 2018; Murthy, Rahi 2014). We also find the wind speed follows the Weibull distribution given as

$$W(v) = A\frac{k}{c}\left(\frac{v}{c}\right)^{k-1} exp\left\{-\left(\frac{v}{c}\right)^{k}\right\}, \tag{3}$$

where k is called the shape parameter, c the scale parameter of the distribution, and k is the failure rate (Murthy, Rahi 2014). Note that A is just the fitting parameter to the number of frequency of histogram.

Dashed line in Fig. 2 shows the probability density $W(v)$ by taking the parameters $A = 10^5$, $c = 11.5$, and $k = 2.1$. Fitting with the histogram is reasonably good. A more accurate comparison between the data and the probability distribution function should be given by the integral form of the histogram producing just the probability (cumulative). Solid (black) and dash-dotted (red) lines in Fig. 2 show the probability calculated from the data (histogram) and the Weibull distribution (red dash line) using the same parameters. Both curves fit well, suggesting that the histogram (and hence the wind speed distribution) follows basically the Weibull distribution.

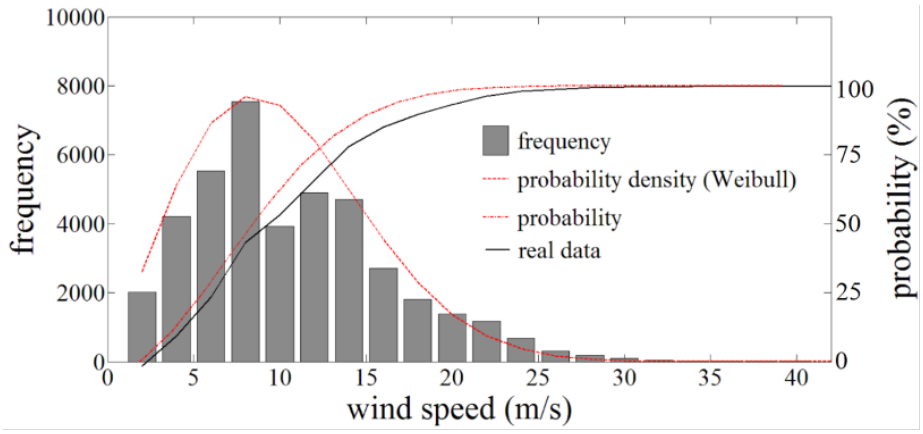

Fig. 2. Wind speed distribution (histogram) and the Weibull distribution

The power spectrum $|v(f)|^2$, obtained from the FFT, is shown in Fig. 3. At higher frequencies, it decreases with increasing frequency f and is approximately given by $1/f^{\alpha}$ by the thin solid line (red). The a-value and its functional origin will be discussed later. At lower frequencies, the spectrum shows a constant, which is often called a *low pass filter* (Belo et al. 2021). At around 10^{-5} Hz, a peak is observed, which corresponds to 1-day period. A 2nd harmonicity (peak) appears at half day cycle. It is not clear whether the presence of the 2nd harmonicity is due to a performance of the FFT or due to actual half-day cycle of the wind nature. We hence ignore the 2nd peak in the present analysis. Interestingly, the feature of $1/f^{\alpha}$ ($\alpha \sim 2$) at high frequencies has been found in the tidal-height spectrum at Dili port (Belo et al. 2021).

As stated already, the discussion of the autocorrelation function $C(\tau)$ may be helpful in understanding the underlying physics of the wind speed, which produces information on the periodicity and the memory of the time of events (Kogan 2008). Fig. 4 shows the autocorrelation functions for the imposed time shift,

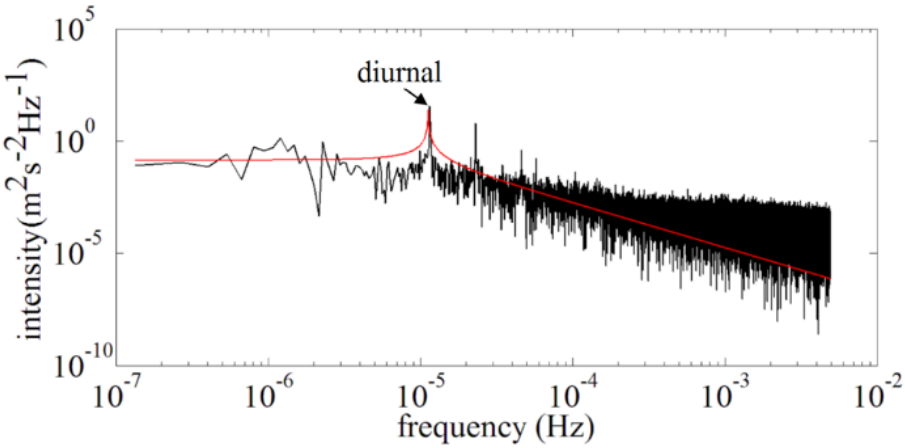

Fig. 3. Power spectrum $|v(f)|^2$ of $v(t)$ (shown in Fig. 1) obtained from the FFT. Solid line (red) is a model prediction of transfer function

(a) τ_{max} = 3.7 × 10^6 s (43 days) and for (b) τ_{max} = 1.8 × 10^5 s (~ two days). Here, we use the correlation time τ (not t) as a time variation. As seen for the $v(t)$ in Fig. 1, $C(\tau)$ shows the periodicity with beat. The time at which $C(\tau)$ is first crossing zero is a characteristic time τ_0 ($C(\tau)$ = 0), which is a measure of the time of losing memory of an event and is estimated to be 2.1 × 10^4 s (~ 6 h). We find the first (positive) peak at 8.7 × 10^4 s (~ 1 day) and the second one at 1.7 × 10^5 s (~ 2 days), indicating that there is a one-day periodicity (diurnal). A slow decrease in $C(\tau)$ with the time-lag around a half day indicates that the wind speed is not strictly periodic (Belu, Koracin 2013). A very slow decay of $C(\tau)$ suggests the presence of another periodic component of a much lower frequency.

Let us discuss the detailed nature of the power spectrum as shown in Fig. 3. As already stated, the power spectrum shows the principal peaks around at 10^{-5} Hz corresponding to the diurnal, and below and above these frequencies, it takes a constant value and is proportional to $1/f^{\alpha}$,respectively. The solid line (α = 2.0) is obtained from the following characteristic of an equivalent LRC electric circuit (EEC) as shown in Fig. 5 (a). The transfer function $H(\omega)$ (Draper et al. 2014), i. e. V_o/V_i for ω (= 2πf), is defined as

$$H(\omega)=\frac{V_o}{V_i}=\frac{\dfrac{R}{1+i\omega CR}}{\dfrac{R}{1+i\omega CR}+i\omega L}=\frac{1}{\left(1-\omega^2 CL\right)+i\omega\dfrac{L}{R}}\equiv\frac{1}{A+iB}\,, \tag{4}$$

where L is the inductance (H), R the resistance (Ω), and C the capacitance (F). A and B, respectively, are given as

$$A=1-\omega^2 CL=1-\frac{\omega^2}{\omega_0^2}\,, \tag{5}$$

$$B=\omega\frac{L}{R}=\omega\tau_c\,, \tag{6}$$

where ω_0 is the resonance frequency given by $1/(CL)^{1/2}$ and τ_c is the relaxation time given by L/R. The absolute value of $H(\omega)$ is then given by

$$\left|H(\omega)\right|=\left(\frac{1}{A^2+B^2}\right)^{\frac{1}{2}}. \tag{7}$$

The solid line shows the K·$|H(f)|$ with L = 2.0 × 10^4 (H), c = 1.0 × 10^4 (F), and R = 1.0 × 10^3 (Ω), where K is just an adjustable parameter (= 3.0 × 10^{-11}) to the data. The $|H(f)|$ takes a constant at low frequencies and is proportional to $1/f^{2.0}$ at high frequencies, with a peak at $2\pi f_0 = (LC)^{-1/2}$. Note, here, that second harmonics ($2f_0$) is not taken into account in the analysis. It is noted that fitting of $|H(f)|$ into the power

 https://www.doi.org/10.33910/2687-153X-2021-2-4-141-148

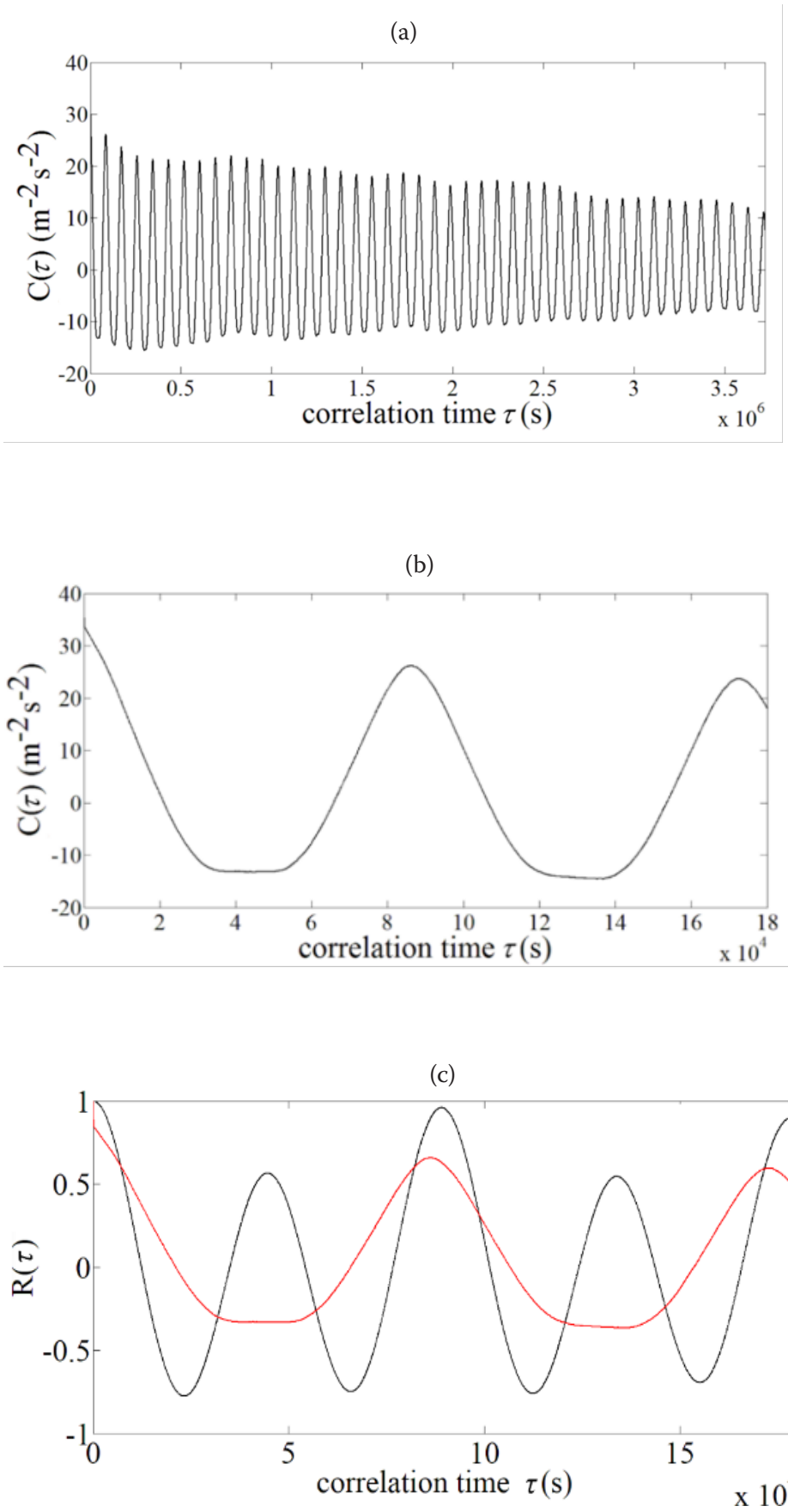

Fig. 4. Autocorrelation function of $v(t)$ for the imposed time shift, (a) $\tau_{max} = 3.7 \times 10^6$ s (43 days), for (b) $\tau_{max} = 1.8 \times 10^5$ s (~ two days) and for (c) tide (black) and wind power (red) for $\tau_{max} = 1.8 \times 10^5$ s (~ two days)

spectrum $|v(f)|^2$ at high frequencies is not good. Mind that the values for all physical parameters do not have any physical meaning, showing only the correspondence to an equivalent electrical circuit. A mechanical system is known to be equivalent to an electrical circuit: mass M (kg) corresponds to L, mechanical resistance R_m (kgs^{-1}) to R, and mechanical compliance C_m (mN^{-1} or $kg^{-1}s^2$) to C (Firestone 1933). Then the L, R, C in Eqs. (5), (6) and (7), can be replaced by these mechanical terms shown in Fig. 5 (b), when we discuss the wind dynamics.

The model predicts $1/f^{\alpha}$ ($\alpha = 2.0$) at higher frequencies with a peak (diurnal), while the actual spectrum shows $\alpha < 2.0$. It should be noted that *fractional kinetics* (*fractional calculus*) is discussed in some relaxation systems (Hilfer 2000; Nigmatullin, Ryabov 1997; Sokolov et al. 2002). The Cole-Davidson type relaxation (Nigmatullin, Ryabov 1997) found empirically in dielectric relaxation should be an example of fractional kinetics, while its origin is still not clear. The $H(\omega)$ can then be modified into

$$H(\omega) = \frac{1}{(A + iB)^{\beta}}, \tag{8}$$

where β ($0 < \beta < 1.0$) is the fractional parameter.

Solid line in Fig. 6 shows the power spectrum $|v(f)|2$ and $K \cdot |H(f)|$ (solid line) obtained from Eqs. (5), (6), and (8) with the parameters $f_0 = 1.13 \times 10^{-5}$ Hz, $\tau_0 = 20$ s, $\beta = 5/6$, and $K = 2.3 \times 10^{-13}$ (see Appendix). $K \cdot |H(f)|$ is proportional to $1/f^{2\beta}$. Note that $2\beta = 5/3$ is the well-known Kolmogorov's parameter on turbulence. We find that the Cole-Davidson type relaxation with $\beta = 5/6$ fits well into the practical power spectrum of the wind power at the present location. It should be mentioned that the wind power

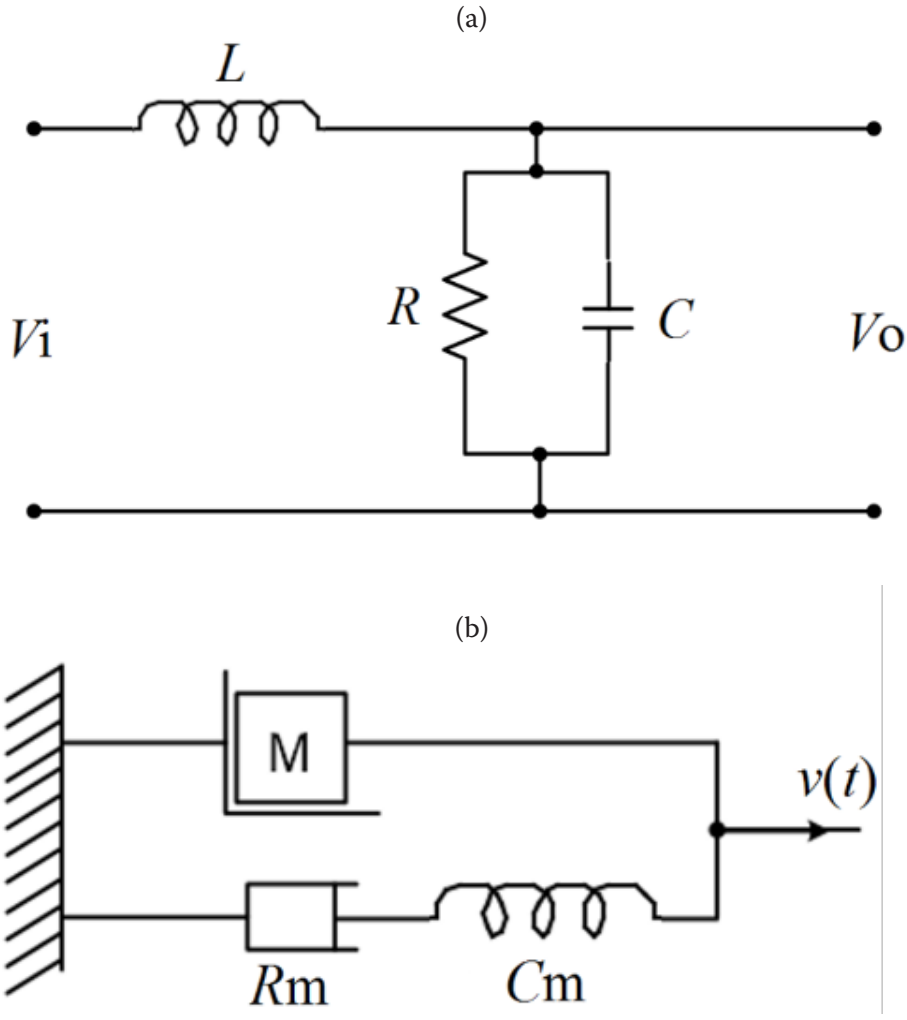

Fig. 5. (a) Equivalent electrical circuit on the wind dynamics, (b) Equivalent mechanical system

 https://www.doi.org/10.33910/2687-153X-2021-2-4-141-148

at the other locations also shows similar behaviour in which $1/f^{5/3}$ (Kolmogorov spectrum) has been reported (Apt 2007). Origin of the fractional dynamics of wind should be related to turbulence in wind nature (meteorological effect). Note in the tide dynamics that the power spectrum of tide in Dili port follows just 1/f at high frequencies, which is completely different from the present wind case. The tide dynamics is dominated only by the gravitational effect without involving the meteorological one (Belo et al. 2021).

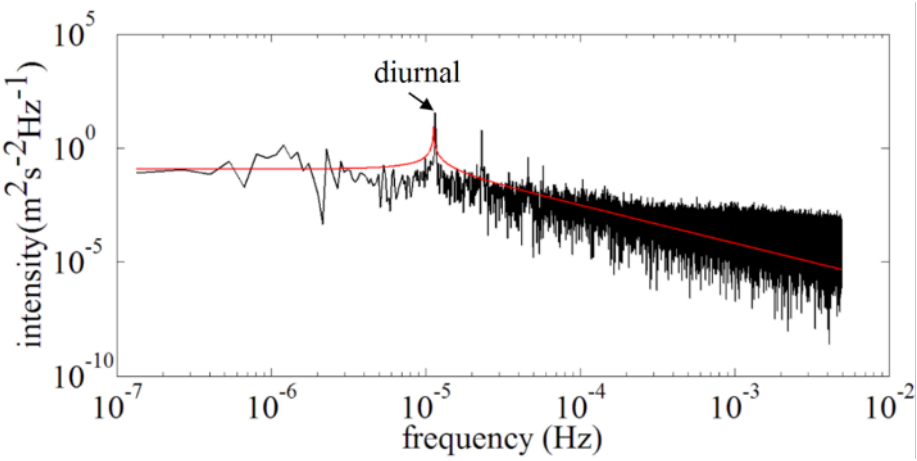

Fig. 6. Power spectrum of $v(t)$ from the FFT. Solid line (red) shows a model prediction (transfer function) of the fractional dynamics of wind power with α = 5/3

Conclusion

The variation of the wind speed during 3 months in time domain at Hera Campus (East Timor) was analysed through the histogram, AF, and FFT. The wind speed was modelled using the Weibull distribution function. The AF in time domain showed roughly a nonexponential decay with one-day periodicity and the correlation disappeared in 6 h. The power spectrum in frequency domain was approximately proportional to $1/f^{5/3}$ at higher frequencies (Kolmogorov spectrum), which was different from the tide dynamics. The Cole-Davidson type relaxation appearing in the wind spectrum should be highly related to turbulence and is related to the fractional dynamics.

Appendix

Equation (10) is solved in the following manner:

$$H(\omega)=(A+iB)^{-\beta}=\left(A^2+B^2\right)^{-\frac{\beta}{2}}e^{-i\left(\beta tan^{-1}\left(\frac{B}{A}\right)\right)}$$

$$=\left(A^2+B^2\right)^{-\frac{\beta}{2}}\left[\cos\left(\beta tan^{-1}\frac{B}{A}\right)-isin\left(\beta tan^{-1}\frac{B}{A}\right)\right],$$

where A and B are given Eqs. (5) and (6), respectively.

Conflict of Interest

The authors declare that there is no conflict of interest, either existing or potential.

Acknowledgement

We would like to thank Professors T. Kobayashi and Y. Takahashi for discussion on the weather focusing.

References

Apt, J. (2007) The spectrum of power from wind turbines. *Journal of Power Sources*, 169 (2), 369–374. https://doi.org/10.1016/j.jpowsour.2007.02.077 (In English)

Belo, A. F., Guterres, R., Pires, A., Shimakawa, K. (2020) Statistical and spectral analysis of wind power in hera campus. *Timorese Academic Journal of Science and Technology*, 3, 22–27. (In English)

Belo, A. F., Sasa, K., Marques, J. M., Shimakawa, K. (2021) Tide level in time and frequency domains at Dili port : Characteristic feature of a Lorentz oscillator. *Physics of Complex Systems*, 2 (1), 41–48. https://www.doi.org/10.33910/2687-153X-2021-2-1-41-48 (In English)

Belu, R., Koracin, D. (2013) Statistical and spectral analysis of wind characteristics relevant to wind energy assessment using tower measurements in complex terrain. *Journal of Wind Energy*, 2013, article 739162. http://dx.doi.org/10.1155/2013/739162 (In English)

Draper, S., Adcock, T. A., Borthwick, A. G., Houlsby, G. T. (2014) An electrical analogy for the Pentland Firth tidal stream power resource. *Proceedings of the Royal Society A*, 470 (2161), article 20130207. https://doi.org/10.1098/rspa.2013.0207 (In English)

Firestone, F. A. (1933) A new analogy between mechanical and electrical systems. *The Journal of the Acoustical Society of America*, 4, 249–267. https://doi.org/10.1121/1.1915605 (In English)

Hasche, B. (2010) General statistics of geographically dispersed wind power. *Wind Energy*, 13 (8), 773–784. https://doi:10.1002/we.397 (In English)

Hilfer, R. (2000) *Applications of fractional calculus in physics*. Singapore: World Cientific Publ., 472 p. https://doi.org/10.1142/3779 (In English)

Joselin Herbert, G. M., Iniyan, S., Sreevalsan, E., Rajapandian, S. (2007) A review of wind energy technologies. *Renewable and Sustainable Energy Reviews*, 11 (6), 1117–1145 https://doi.org/10.1016/j.rser.2005.08.004 (In English)

Kogan, Sh. (2008) *Electronic noise and fluctuations in solids*. Cambridge: Cambridge University Press, 367 p. (In English)

Matsfelt, J., Davidson, L. (2021) Large eddy simulation: A study of clearings in forest and their effect on wind turbines. *Wind Energy*. [Online]. https://doi.org/10.1002/we.2637 (accepted 28.08.2021). (In English)

Murthy, K. S. R., Rahi, O. P. (2014) Estimation of Weibull parameters using graphical method for wind energy applications. In*: 18th National power systems conference (NPSC–2014)*. Guwahati: IEEE Publ., pp. 1–6. https://www.doi.org/10.1109/NPSC.2014.7103858 (In English)

Nigmatullin, R. R., Ryabov, Ya. E. (1997) Cole-Davidson dielectric relaxation as a self-similar relaxation process. *Physics of Solid State*, 39 (1), 87–90. https://doi.org/10.1134/1.1129804 (In English)

Norheim, I., Pudjianto, D. (2007) Method for assessing impact of large-scale wind power integration on reserves. *Wind Energy*, 11 (1), 85–96. https://doi.org/10.1002/we.252 (In English)

Papoulis, A. (1962) *The fourier integral and its applications*. New York: McGraw-Hill Publ., 318 p. (In English)

Sokolov, I., Klafter, Y., Blumen, A. (2002) Fractional kinetics. *Physics Today*, 55 (11), 48–54. https://doi.org/10.1063/1.1535007 (In English)

Wan, Y., Bucaneg , D. Jr. (2002) Short-term power fluctuations of large wind power plants. *Journal of Solar Energy Engineering*, 124 (4), 427–431. https://doi.org/10.1115/1.1507762 (In English)

Zonst, A. E. (2004) *Understanding the FFT applications: A tutorial for students & working engineers*. 2nd ed., rev. Titusville: Citrus Press., 280 p. (In English)

Condensed Matter Physics. Dielectric Physics

UDC 538.9 https://www.doi.org/10.33910/2687-153X-2021-2-4-149-156

Nature and mechanisms of relaxation processes in biocompatible polylactide films

Yu. A. Gorokhovatskiy[1], E. A. Karulina[1], D. A. Ignatyeva[2]✉

[1] Herzen State Pedagogical University of Russia, 48 Moika Emb., Saint Petersburg 191186, Russia
[2] Peter the Great St. Petersburg Polytechnic University, 29 Polytechnicheskaya Str., Saint Petersburg 195251, Russia

Authors

Yuriy A. Gorokhovatskiy, ORCID: 0000-0001-5085-2525, e-mail: yurig@fromru.com

Elena A. Karulina, ORCID: 0000-0001-9604-4769, e-mail: karulina@mail.ru

Daria A. Ignatyeva, e-mail: ignatyeva.daria92@gmail.com

For citation: Gorokhovatskiy, Yu. A., Karulina, E. A., Ignatyeva, D. A. (2021) Nature and mechanisms of relaxation processes in biocompatible polylactide films. *Physics of Complex Systems*, 2 (4), 149–156. https://www.doi.org/10.33910/2687-153X-2021-2-4-149-156

Received 6 October 2021; reviewed 15 October 2021; accepted 15 October 2021.

Funding: The research was supported by the Ministry of Education of the Russian Federation as part of state task (Project No. FSZN-2020-0026).

Abstract. The results of a TSRSP study of the electret properties of initial PLA films and PLA-based composite films with various hydrophilic nanoscale fillers are presented. It is shown that the introduction of a filler into the composite matrix changes the relaxation mechanism and leads to an improvement in the electret state stability in the PLA-based composite samples. The maximum possible value of the electret state stability in PLA-based composite film is provided by the proper electreting mode.

The nature and mechanism of relaxation, as well as the stability of the electret state, is obtained by the presence of charge-dipole centres in the polymer structure. The presence and distribution form of the charge-dipole centres in the polymer matrix of PLA composites was confirmed by FTIR-spectroscopy and the attenuated total reflectance (ATR) method.

***Keywords*:** polylactide, polymer composite, charge-dipole centres, electret state stability, thermal activation spectroscopy, FTIR-spectroscopy, attenuated total reflectance (ATR).

Introduction

In the modern world, food preservation is impossible without the right packaging material. One way of advancing the field is the development of new polymeric materials with special properties. Such packages are called “active packaging materials”. Active packaging materials refer to packaging systems used for food, pharmaceuticals and some other types of products (Galikhanov et al. 2005; 2014). They can contain various absorbents of moisture and odours, as well as antimicrobial enzymes and additives that have a targeted effect on products they contact (Fedotova et al. 2010).

The creation and comprehensive study of “active packaging materials” is of great interest; since the additive is not introduced into products, but into the structural matrix of a polymer film, it allows prolonging the products’ shelf life in such a polymer shell, controlling freshness and increasing the safety and convenience (Fedotova et al. 2010).

Another equally interesting and important way of research and development is the creation of biodegradable materials. Earlier the efforts of scientists aimed at creating polymers resistant to various kinds of influences. Now the opposite trend is being formed. Biodegradable and biocompatible polymeric materials are increasingly being developed. However, such materials are inferior in their properties

to traditional plastics, but the fact that they are biodegradable is their main advantage, since they are capable of decomposing into safe components via the action of biological environmental factors (Fomin, Guzeev 2001; Legonkova 2006). Interest in such technologies is growing due to the increase in human consumption of disposable products.

The most promising polymer is polylactide (PLA). PLA is a biodegradable, thermoplastic biopolymer, the monomer of which is lactic acid. It is mainly obtained for medical purposes, as well as for the manufacture of packaging materials and products with a short service life (Pihlajamaki et al. 2006). PLA is completely biodegradable in 45 days under industrial composting conditions (Ermolovich et al. 2005; Stein 1992).

Combining these two ways of investigations could lead to the creation of "active biodegradable packaging" based on PLA. Such packaging could allow prolonging shell life of food and maintaining its operational characteristics only during the period of consumption. Then they undergo physicochemical and biological transformations under the influence of the Earth's biosphere.

However, it is known that the shell life of food in PLA films is limited (Ignatyeva et al. 2015b). Possible ways to increase this time are the creation of polymer-based composites by introducing additional inclusions into the structure of the polymer matrix, as well as advance electreting of the polymer sample. Pre-electreting in the corona discharge field enhances the bactericidal properties of polymer films. The electret process has an inhibitory effect on microorganisms in food (Galikhanov et al. 2008). Thus, this makes it possible to use pre-electreted biodegradable polymer films as "active packaging materials".

Experimental procedure

In this paper, we have investigated the biodegradable initial PLA films and PLA-based composites with various hydrophilic nanoscale dispersed fillers (silicon dioxide, barium titanate, etc.). This research involved studying two types of PLA samples with different thickness: thin films (about 40 μm) and thick films (more than 180 μm).

In order to study the structure and basic electrophysical phenomena of PLA films (the processes of transfer, accumulation and relaxation of charge), as well as to refine the proposed model of the electret state stability and to estimate the parameters of relaxation processes, a combination of experimental methods was used. Combined application of FTIR-spectroscopy and thermoactivation spectroscopy methods (in particular, the method of thermally stimulated relaxation of the surface potential (TSRSP)) makes it possible to obtain detailed information on the nature and mechanisms of relaxation processes in PLA films.

In order to investigate the electret state stability by the TSRSP method, the PLA samples were preliminarily electreted for 10 minutes in a field of positive and negative corona discharges at room temperature and at a higher temperature (about 55–60 °C).

Results and discussion

Relaxation of the surface potential in the initial PLA films

Fig. 1 demonstrates the TSRSP curves of the initial PLA films (at the same heating rate) charged in the unipolar corona of positive and negative signs. The inflection point temperature on the TSRSP curve characterises the temperature stability of the electret state. In this study, this temperature is approximately 45–50 °C (Fig. 1), which indicates low electret stability. The sign of the surface charge for the PLA samples corresponded to the accumulation of homocharge.

Furthermore, it should be noted that the TSRSP curves obtained for different signs of the corona discharge are practically identical. This fact allows suggesting that the relaxation of the surface potential in the initial PLA films (without a filler) is preconditioned by the neutralisation of the homocharge. It is a characteristic feature of the charge relaxation process introduced with the corona effect due to the bulk conductivity of the initial PLA films (Ignatyeva et al. 2015a).

The TSRSP method made it possible to reveal that the initial PLA films (without fillers) have low electret properties. The electret state storage time of the initial PLA films was also estimated by direct measurements of the surface potential at room temperature (Fig. 2). Fig. 2 demonstrates that the electret state storage time of the initial PLA film is approximately 15 hours. This indicates the shell life of food products in electreted initial PLA packages is limited.

 https://www.doi.org/10.33910/2687-153X-2021-2-4-149-156

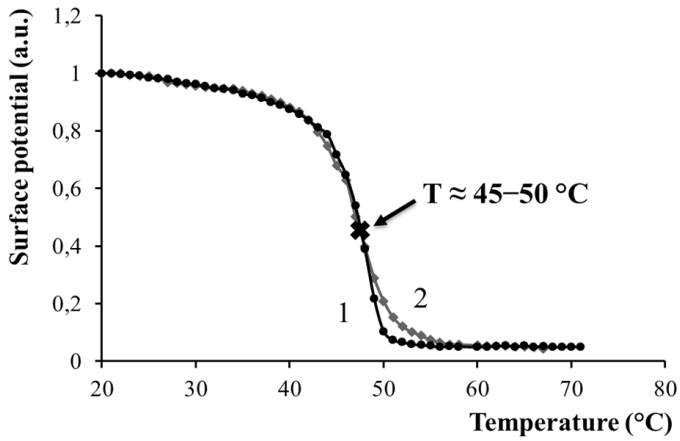

Fig. 1. TSRSP curves of initial PLA film (without fillers), electreted in the field of negative (curve 1) and positive (curve 2) corona discharge

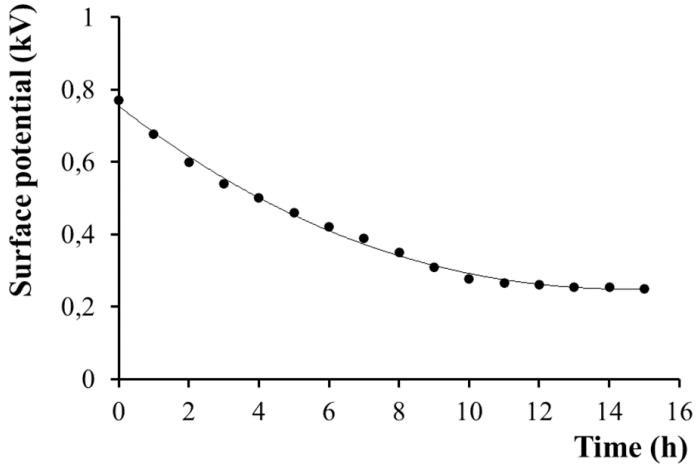

Fig. 2. Dependence of the surface potential on the electret state storage time of the initial PLA film

In studies (Gorokhovatskiy et al. 2017; Ignatyeva et al. 2015b), it was suggested that the structure of aliphatic polyesters may contain quasimolecular complexes, such as charge-dipole centres. Charge-dipole centres have a dual nature. On the one hand, due to the dipole structure, they can take part in polarisation. On the other hand, such centres are formed because of the interaction of charge carriers with H_2O, O_2, H_2 molecules dissolved in the polymer structure, as well as with structural defects, such as traps ("sticking centres") of charge carriers, thereby affecting the conductivity of polymeric materials.

Thus, it seems reasonable to suppose that the low electret state stability in the initial PLA films, which is preconditioned by increased bulk conductivity, is related to the presence of charge-dipole centres in the structure of the PLA sample (Gorokhovatskiy et al. 2017; Ignatyeva et al. 2015a; 2015b).

Relaxation of the surface potential in PLA-based composite films with hydrophilic nanoscale fillers

It was assumed that the introduction of a hydrophilic nanoscale filler (such as silicon dioxide, barium titanate, etc.) into the PLA polymer matrix would facilitate the capture of water by the filler particles. This process, in turn, should lead to a decrease in the concentration of charge-dipole centres. Thus, the conductivity of the polymer material should decrease and the electret properties of the composite should improve.

In (Ignatyeva et al. 2015a), it was shown that in PLA-based composite films with a hydrophilic nanoscale filler silicon dioxide (SiO_2) the decrease in the surface potential is determined by the release of the captured charge from near-surface traps. The energy depth of traps for charge carriers of opposite signs is different,

since relaxation of the surface potential occurs at different temperatures. This is possible if the bulk conductivity in the PLA-based composite films is significantly lower than in the initial PLA films.

The relaxation of the surface potential has a two-stage form for PLA-based composite films (Ignatyeva et al. 2015a). The relaxation in low-temperature area (about 55 °C) occurs due to the reorientation of polar structures in the internal field of a side charge. In the high-temperature area, the relaxation of the surface potential for a PLA-based composite film, electreted in the positive corona discharge, occurs at T ≈ 80 °C, and in the negative corona discharge at T ≈ 70 °C. The asymmetry of the TSRSP curves is explained by the release of charges from the trapping centres, which are characterised by different parameters (activation energy and frequency factor) for positive and negative carriers.

Since the relaxation of the surface potential has a two-step form, preliminary electreting in the field of a corona discharge at a temperature of 55–60 °C, followed by cooling in a corona discharge to room temperature, was carried out. Subsequently, the surface potential of the sample was measured.

Fig. 3 shows the TSRSP curves of the initial PLA samples and PLA-based composite pre-electreted at a high temperature (55–60 °C) charged at the same heating rate in a positive corona discharge.

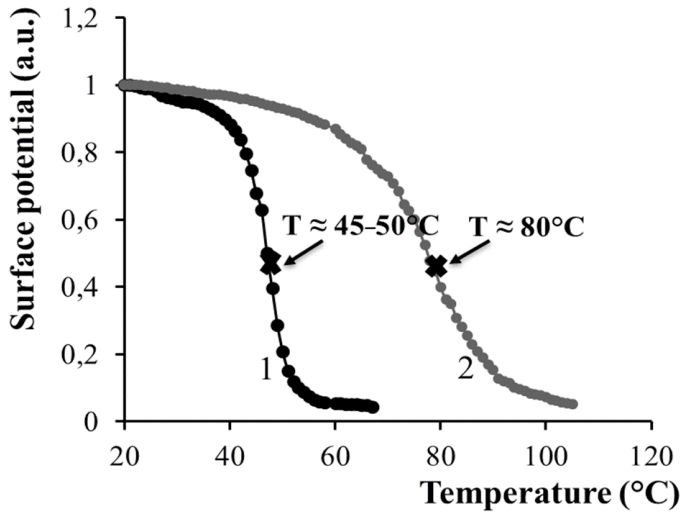

Fig. 3. TSRSP curves of samples charged in a positive corona discharge at the same heating rate: the initial PLA film (curve 1) and the PLA-based composite film (with 2% SiO_2) pre-electreted at a high temperature (55–60 °C, curve 2)

Thus, the introduction of a hydrophilic nanoscale filler reduced the concentration of charge-dipole centres, as well as preliminary preparation of the composite sample (advance electreting in a positive corona discharge at a high temperature) made it possible to increase the temperature electret stability from 50 °C to 80 °C (Fig. 3).

This procedure also allows increasing the temporal electret stability of the PLA-based composite (Fig. 4). It was experimentally revealed that the electret state storage time of the PLA-based composite sample at room temperature exceeds 4 months.

This result makes it possible to recommend PLA-based composite films with nanoscale filler SiO_2 (vol. 2%) pre-electreted at a high temperature (55–60 °C) for practical use as biodegradable active packaging.

The IR-transmittance spectra and the ATR spectra. Model of electret stability in initial PLA films and PLA-based composite films

The presence of charge-dipole centres in thin PLA films (about 40 μm) was established experimentally using the method of FTIR-spectroscopy (Ignatyeva et al, 2015b). Curve 1 (Figs. 5–6) corresponds to the IR-transmission spectrum of thin PLA film. The bands determined by the presence of charge-dipole

 https://www.doi.org/10.33910/2687-153X-2021-2-4-149-156

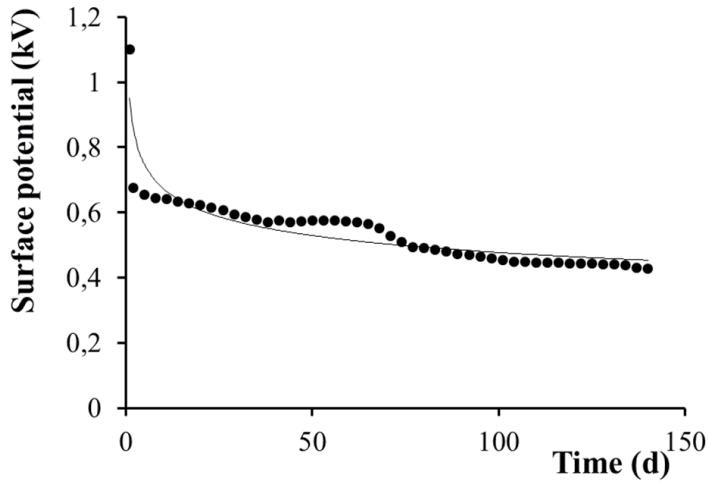

Fig. 4. Dependence of the surface potential on the electret state storage time of the PLA-based composite (with 2% SiO_2) pre-electreted at a high temperature (55–60 °C)

centres in the structure (1501 cm^{-1}, 1561 cm^{-1}, 1591 cm^{-1}, 3055 cm^{-1}) are presented in Figs. 5 and 6 (Ignatyeva et al. 2015b).

Lowering the bulk conductivity and, therefore, increasing the electret state stability is known to be achieved via the introduction of hydrophilic nanoscale fillers into the polymer matrix of the sample (Gorokhovatskiy et al. 2018).

This study presents the IR-transmission spectrum of the PLA-based composite with hydrophilic nanoscale barium titanate ($BaTiO_3$) (curve 2, Figs. 5–6). The intensity of the absorption bands corresponding to charge-dipole centres decreases due to the introduction of $BaTiO_3$ (Figs. 5–6). The particles of $BaTiO_3$ filler capture and bind water molecules in the near-surface regions of polymer matrix of PLA, which leads to the reduction of the concentration of charge-dipole centres in the PLA-based composite structure.

The fact of a decrease in the concentration of charge-dipole centres confirms the results obtained by the TSRSP method (relaxation mechanism and the model of the charge-dipole centres) and leads to an increase in the electret state stability.

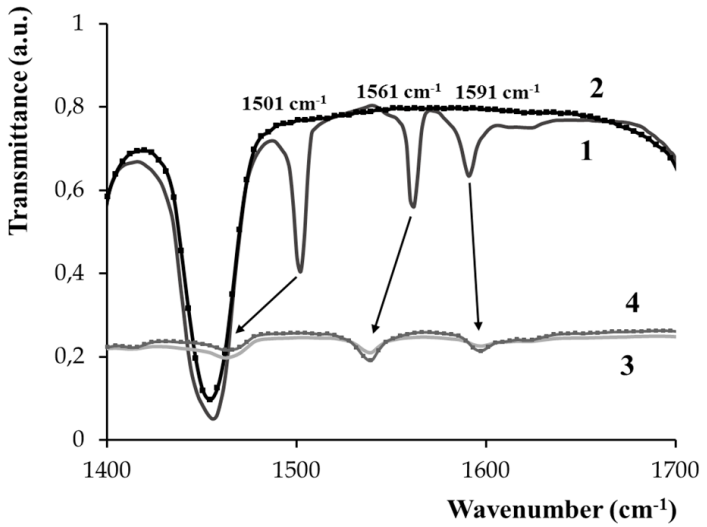

Fig. 5. The IR-transmittance spectra of the initial PLA (curve 1) and the PLA-based composite + $BaTiO_3$ (curve 2); the ATR spectra of the initial PLA (curve 3) and the PLA-based composite + $BaTiO_3$ (curve 4) in the range of wavenumbers 1400–1700 cm^{-1}

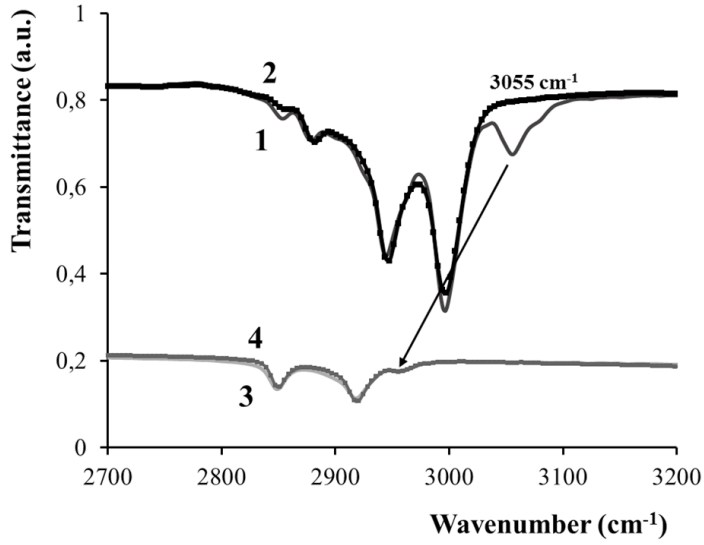

Fig. 6. The IR-transmittance spectra of the initial PLA (curve 1) and the PLA-based composite + $BaTiO_3$ (curve 2); the ATR spectra of the initial PLA (curve 3) and the PLA-based composite + $BaTiO_3$ (curve 4) in the range of wavenumbers 2700–3200 cm^{-1}

The experimental data of the TSRSP and FTIR-spectroscopy of thin PLA films (about 40 μm) are in good agreement with the proposed model of charge-dipole centres. However, during the study of thick PLA films (more than 180 μm) this model turned out to be not entirely correct.

Specifically, the absorption bands corresponding to charge-dipole centres are strongly weakened or not observed at all in the initial thick PLA films on the IR-transmission spectra (Gorokhovatskiy et al. 2019). It casts doubt on the fact of charge-dipole centres presence in these films and the proposed model. That is why the ATR method for the research composite PLA-based films with different thickness was used.

The presence of absorption bands corresponding to charge-dipole centres in the initial thick PLA films (curve 3, Figs. 5–6) was revealed by the ATR method. Previously, the presence of these bands in the IR-transmission spectra of a thick PLA films was not established, but these bands are presented in the ATR spectra. The ATR spectra of PLA-based composites with $BaTiO_3$ (curve 4, Figs. 5–6) also demonstrate bands associated with charge-dipole centres.

It is worth mentioning a shift of all absorption bands of ATR spectra to shorter region of wavenumbers (about 100 cm^{-1}).

Absorption bands associated with charge-dipole centres are present in all ATR spectra: both in the spectra of the initial PLA and in the spectra of PLA-based composites with different hydrophilic nanoscale dispersed fillers.

These experimental results obtained by the ATR method made it possible to trace the presence of charge-dipole centres in all samples of PLA and PLA-based composites (thin and thick films). This allows us to conclude that these centres are predominantly formed in the near-surface regions via constant contact with the molecules of atmosphere. It can also be assumed that the distribution of these centres has a saddle-like shape. A large concentration of these centres is observed in the near-surface zone, and decreases from the centre to the periphery.

Conclusion

All the presented results obtained by using a set of research methods allow us to draw the following conclusions.

The presence of charge-dipole centres in the initial thin PLA films and their disappearance in PLA-based composite films with a hydrophilic nanoscale filler is confirmed by the method of FTIR-spectroscopy. A decrease in the intensity of absorption bands corresponding to charge-dipole centres in the IR-transmission spectra is connected with capture of free molecules of water, oxygen, and hydrogen by the filler particles. Considering the limited possibility of registering the charge-dipole centres

 https://www.doi.org/10.33910/2687-153X-2021-2-4-149-156

by FTIR-spectroscopy in thick PLA films, the ATR method was used, which also confirmed their presence in the structure of the initial thin and thick PLA films and PLA-based composites. The distribution of the charge-dipole centres in the polymer film has a saddle-like shape, and the maximum concentration is observed in the near-surface zone, decreasing from the centre to the periphery.

The model of the charge-dipole centres makes it possible to explain the nature and mechanisms of relaxation, as well as the stability of the electret state, in the initial PLA films and PLA-based composites, which were obtained by the TSRSP method.

The low stability of the electret state in the initial PLA films was established, The increased bulk conductivity in the initial PLA films is associated with the formation of charge-dipole centres in the polymer structure. The temperature of electret state stability in the initial PLA films is about 45–50 °C.

The TSRSP method allows establishing two areas of relaxation in PLA-based composite films:

- low-temperature area (T ≈ 55 °C), which is connected with the reorientation of polar structures in the homocharge field;
- high-temperature area (T ≈ 70–80 °C) (depending on the sign of the corona discharge), which is related to relaxation of the surface potential via ejection of the charge from deep near-surface traps.

Moreover, the proper electreting mode (allowing to increase the electret state stability) for PLA-based composite films was presented. The temperature stability of the electret state in pre-electreted at a high temperature (55–60 °C) PLA-based composite films in the field of a positive corona discharge is about 80 °C.

It was experimentally revealed that the electret state storage time of the PLA-based composite film at room temperature exceeds 4 months, which makes it possible to recommend it as an "active packaging material".

Conflict of Interest

The authors declare that there is no conflict of interest, either existing or potential.

References

Ermolovich, O. A., Makarevich, A. V., Goncharova, E. P., Vlasova, G. M. (2005) Metody otsenki biorazlagaemosti polimernykh materialov [Methods for analyzing of biodegradability of polymeric materials]. *Biotekhnologiya — Biotechnology*, 4, 47–54. (In Russian)

Fedotova, O. B., Myalenko, D. M., Shalaeva, A. V. (2010) "Aktivnaya upakovka" iz polimernykh materialov ["Active packing" from polymeric materials]. *Pishchevaya promyshlennost' — Food Processing Industry*, 1, 22–23. (In Russian)

Fomin, V. A., Guzeev, V. V. (2001) Biorazlagaemye polimery, sostoyanie i perspektivy ispol'zovaniya [Biodegradable polymers, the state and prospects of use]. *Plasticheskie massy*, 2, 42–46. (In Russian)

Galikhanov, M. F., Borisova, A. N., Deberdeev, R. Ya., Krynitskaya, A. Yu. (2005) Aktivnaya upakovka dlya masla [Active packing for oil]. *Pishchevaya promyshlennost' — Food Processing Industry*, 7, 18–19. (In Russian)

Galikhanov, M. F, Guzhova, A. A, Borisova, A. N. (2014) Effect of active packaging material on milk quality. *Bulgarian Chemical Communications*, 46 (Special Issue B), 142–145. (In English)

Galikhanov, M. F, Zhigaeva, I. A., Minnakhmetova, A. K., Deberdeev, R. Ya. (2008) Izuchenie biorazlagaemosti elektretnykh polimernykh materialov [Biodegradability of electret polymer materials]. *Zhurnal prikladnoj khimii — Russian Journal of Applied Chemistry*, 81 (7), 1178-1181. (In Russian)

Gorokhovatskiy, Yu. A., Galikhanov, M. F., Ignatyeva, D. A. et al. (2017) Charge relaxation mechanisms in composite films based on polylactide. *Humanities and Science University Journal*, 27, 46–55. (In English)

Gorokhovatskiy, Yu. A., Chistyakova, O. V., Karulina, E. A. et al. (2019) The detection of charge-dipole centers in composites based on polylactide by attenuated total reflectance method. In: *International conference on electrical engineering and photonics (EExPolytech–2019)*. Saint Petersburg: IEEE Publ., pp. 217–219. https://doi.org/10.1109/EExPolytech.2019.8906796 (In English)

Gorokhovatskiy, Yu. A., Ignatyeva, D. A., Sotova, Yu. I. (2018) Electret effect in composite polylactide based films with hydrophilic nanodispersed fillers. In: *International conference on electrical engineering and photonics* (*EExPolytech–2018)*. Saint Petersburg: IEEE Publ., pp. 192–193. https://doi.org/10.1109/EExPolytech.2018.8564406 (In English)

Ignatyeva, D. A., Gorokhovatskiy, Yu. A., Karulina, E. A. et al. (2015a) Termostimulirovannaya relaksatsiya poverkhnostnogo potentsiala v kompozitnykh plenkakh na osnove polilaktida s nanodispersnym napolnitelem aerosilom [Thermally stimulated relaxation of the surface potential in composite films based on polylactide

with nanodispersed aerosil filler]. *Vestnik Tekhnologicheskogo universiteta — Bulletin of the Technological University*, 18 (18), 61–64. (In Russian)

Ignatyeva, D. A., Karulina, E. A., Chistyakova, O. V. (2015b) Mekhanizm relaksatsii elektretnogo sostoyaniya v plenkakh polilaktida s dispersnym napolnitelem [The mechanism of electret state relaxation in polylactide films containing dispersed filler]. *Izvestia Rossijskogo gosudarstvennogo pedagogicheskogo universiteta im. A. I. Gertsena — Izvestia: Herzen University Journal of Humanities & Sciences*, 173, 39–45. (In Russian)

Legonkova, O. A. (2006) Eshche raz o biorazlozhenii polimernykh materialov [Once again about the biodegradation of polymer materials]. *Tara i upakovka — Package and Packaging Magazine*, 2, 57–58. (In Russian)

Pihlajamaki, H., Bostman, O., Tynninen, O., Laitinen, O. (2006) Long-term tissue response to bioabsorbable poly-l-lactide and metallic screws: An experimental study. *Bone*, 39 (4), 932–937. https://doi.org/10.1016/j.bone.2006.04.009 (In English)

Stein, R. S. (1992) Polymer recycling: opportunities and limitations. *Proceedings of the National Academy of Sciences of the United States of America*, 89, 835–838. https://doi.org/10.1073/pnas.89.3.835 (In English)

Condensed Matter Physics. Dielectric Physics

UDC 536.4 https://www.doi.org/10.33910/2687-153X-2021-2-4-157-164

Analysis of the TSD spectra of polymers near the glass transition temperature using the fractional purification method

N. S. Shabanova✉[1], D. E. Temnov[1]

[1] Herzen State Pedagogical University of Russia, 48 Moika Emb., Saint Petersburg 191186, Russia

Authors

Natalia S. Shabanova, ORCID: 0000-0001-9844-0116, e-mail: natashshabanov@yandex.ru

Dmitry E. Temnov, ORCID: 0000-0002-9560-4346, e-mail: detem@yandex.ru

For citation: Shabanova, N. S, Temnov, D. E. (2021) Analysis of the TSD spectra of polymers near the glass transition temperature using the fractional purification method. *Physics of Complex Systems*, 2 (4), 157–164. https://www.doi.org/10.33910/2687-153X-2021-2-4-157-164

Received 24 September 2021; reviewed 4 October 2021; accepted 4 October 2021.

Funding: The research was supported by the Ministry of Education of the Russian Federation as part of a state task (project No. FSZN-2020-0026).

Abstract. In this work, the thermally stimulated spectroscopy methods are applied to PET films exposed to UV rays for the analysis of electrically active defects parameters in these materials, such as activation energy (E_a) and relaxation time, or frequency factor (ω). To obtain these parameters the methods of thermally stimulated currents and thermally stimulated currents thermal sampling were used. To determine the relaxation parameters using the methods of thermally stimulated currents, various mathematical methods of data processing were used. The Eyring equation and the compensation law were found to be the most correct for PET films. The value of the activation energy determined with their help for the PET exposed to UV rays turned out to be 1.07 eV, and the value of effective frequency factor $\omega = 1/\tau_0 = 5 \times 10^{10}$ c^{-1}.

Keywords: electrets, polyethylene terephthalate, thermally stimulated depolarisation currents, thermally stimulated depolarisation currents thermal sampling.

Introduction

Methods of thermal analysis have been widely used since the 1970s due to the highly informative results. Due to its applicability to a wide range of dielectrics, various interpretations of current methods are of particular interest, allowing us to determine such parameters of electrically active defects in these materials as activation energy (E_a) and relaxation time, or frequency factor (ω), as well as to draw conclusions about the nature of relaxation processes and changes in the thermodynamic characteristics of the system.

The paper analyses the results of a study of polyethylene terephthalate (PET) films by the methods of thermally stimulated currents (TSC) and thermally stimulated currents thermal sampling (method of fractional purification) (TSC-TS), conclusions are drawn about the effectiveness of various methods for processing experimental results obtained by these methods in the field of polymer glass transition temperature.

Materials and methods

TSC and TSC-TS methods

The thermally stimulated relaxation currents method (TSC) in the short-circuit mode with linear cooling involves the following techniques: a sample placed between two electrodes (i. e., being in the short-circuit mode) is polarised at a temperature higher than the glass transition temperature. Then the sample is cooled with an applied field to "freeze" the resulting state. After that, the field is removed and the object of study is heated according to a linear law (Fig. 1).

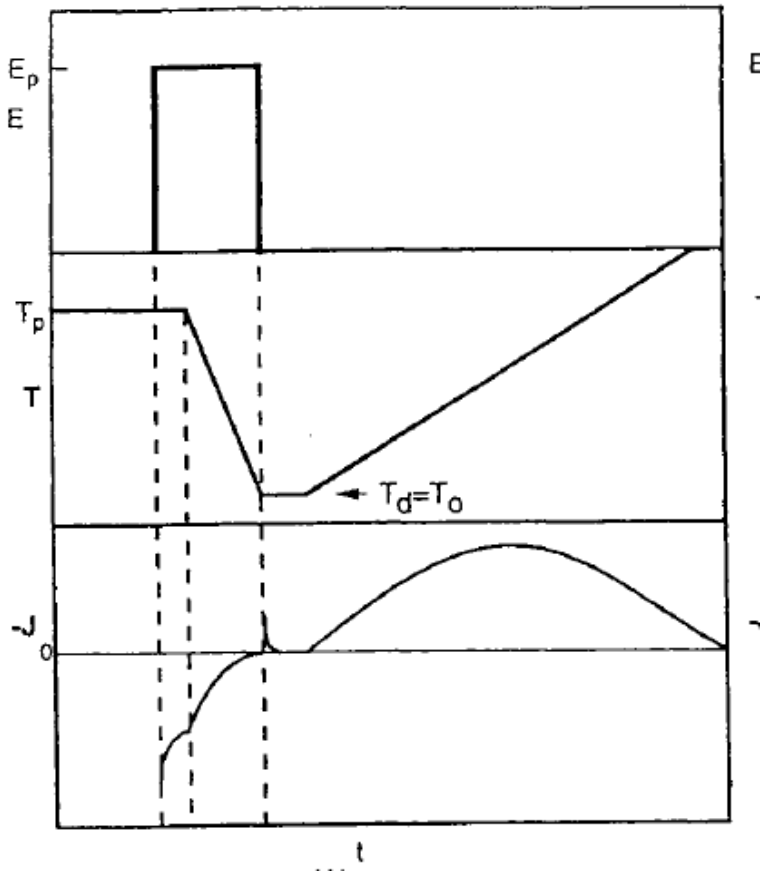

Fig. 1. Mode of operation of the TSC method

A thermally stimulated depolarisation current flows in a circuit. By taking readings using an electrometer and a thermocouple, the current dependence on temperature is obtained. On the graphs of these dependencies, it is possible to identify peaks; their height and location provide information about the mechanism of electrical relaxation and the parameters of electrically active defects. This method sometimes indirectly allows us to calculate the change in the entropy of the system by abnormally high values of the frequency factor and activation energy (Shabanova et al. 2020).

The fractional purification mode (TSC-TS method) is largely similar to the previous mode (TSC). The initial high temperature at the polarised sample is also selected. Then the cooling begins to a temperature, usually denoted by the depolarisation temperature, which does not differ too much from the highest temperature (T_{max}). Thus, the polarisation takes place in a narrow "window" of temperatures, which allows us to observe only those processes and transitions that fall into this window. Then the sample is cooled with the field turned off to the "freezing" temperature (Fig. 2) and after that the dependence of the TSC-TS current on the temperature during heating is removed. The fractional purification method provides a unique opportunity to determine the nature of complex transitions in compounds

 https://www.doi.org/10.33910/2687-153X-2021-2-4-157-164

(this is especially interesting in cases where the transitions overlap and it is important to identify each transition separately).

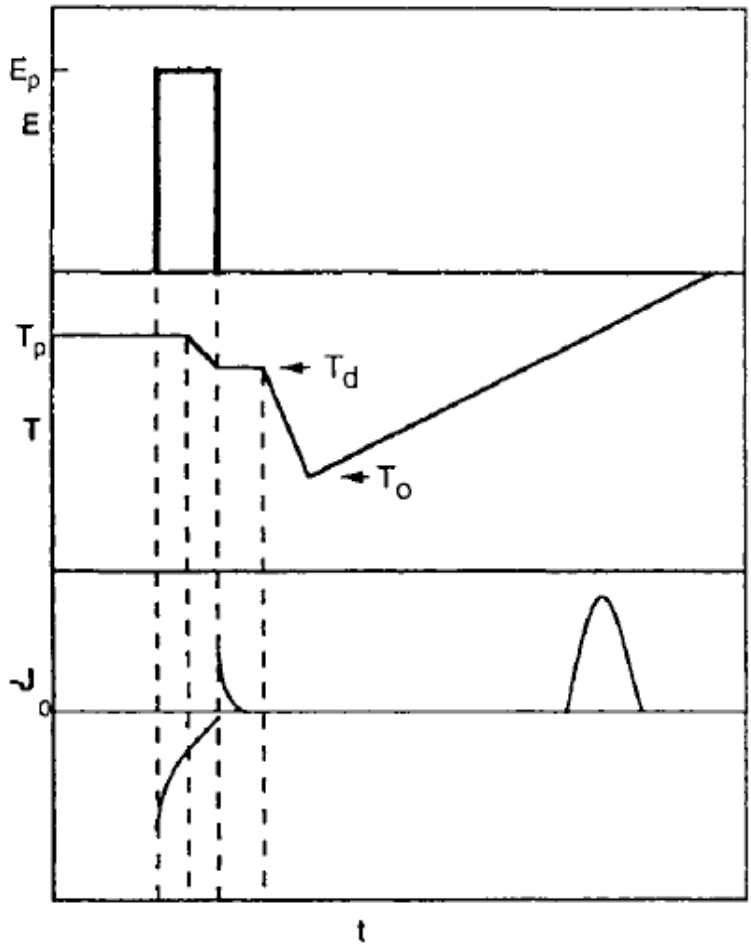

Fig. 2. Mode of operation of the TSC-TS method

In the experimental part of the work, films of polyethylene terephthalate with a thickness of 30 microns were used. PET is a polymer that is a complex thermoplastic polyester of terephthalic acid and ethylene glycol with a glass transition temperature in the region of 80 °C. PET films are a composition consisting of amorphous and crystalline phases. PET in the amorphous state is characterized by a mutual disorderly arrangement of chains of macromolecules with single separate formations of an ordered structure. The crystal state of PET is characterised by the presence of crystallites in the material, i. e. folded bundles of macromolecules in the form of folded bundles. The size of the crystallites in the films is about 5–10 nm, and the degree of crystallinity is about 40–50%.

Calculation methods

To determine the relaxation parameters using the methods of thermally stimulated currents, several mathematical data processing methods may be used. If the polarisation occurred during continuous linear cooling, the method of varying the heating rates (the Bogan-Butte method), the Tikhonov regularisation method or the initial rise method (the Garlick-Gibson method) is used. The first two methods correctly determine the parameters of electrically active defects in the case of a single relaxation in the temperature range that does not affect the glass transition region. The method of initial rise a priori uses values in the temperature range below the glass transition, but it is the least informative and accurate.

In addition, according to the obtained data, mathematical modelling alone is seldom enough to separate non-cooperative processes, and often this task remains unresolved in principle.

The Garlick-Gibson method is based on the fact that at sufficiently low temperatures, the change in charge carriers localised at the capture centres is small compared to the relative change in the concentration of free charge carriers. As shown by theoretical studies at sufficiently low temperatures ($T \approx T_0$), the nature of the dependence of the depolarisation currents does not depend either on the order of the kinetics of the relaxation process or on the heating rate. Thus, in the initial section, the TSD current curves have an exponential dependence on temperature and have the form:

$$j(T) \simeq j_0 e^{-\frac{W}{kT}} \tag{1}$$

So, if we construct the initial section of the current obtained by TSC method in the Arrhenius coordinates ($\ln j \sim 1/kT$), the dependence is linearised. The slope of such a straight line enables calculation of the activation energy.

Tikhonov's method of regularising algorithms provides information about the functions of the activation energy distribution of electrically active defects. This method is based on solving the problem of finding the distribution function of the activation energy for given experimental current values. This problem is incorrect according to Hadamard (small errors at the input give large errors in the results) and is solved by the proposed Tikhonov numerical method. The solution algorithm is described in detail in (Gorohovatskij, Temnov 2007).

The advantages of this method are that it allows us to solve a one-dimensional problem finding a distribution function. This method also takes into account the order of kinetics, but it will be suitable for solving the problem only within the strict framework of a certain model and will give erroneous values when going beyond this framework (for example, this method is not sensitive to changes in entropy and it is impossible to separate such processes with its help).

For an ideal Debye relaxation with a single relaxation frequency, the relaxation times $\tau(T)$ can be obtained from the experimental TSC-TS spectra (the method of thermal dots or fractional purification) using the standard Bucci-Fieschi-Guidi method (Bucci et al. 1966) or the "BFG" method. The relaxation times $(\tau(T))$ for a single Debye relaxation are determined by the equation (Bucci et al. 1966; van Turnhout 1971):

$$\tau(T) = \frac{P(T)}{J(T)}, \tag{2}$$

where $P(T)$ is the remaining polarisation at an arbitrary temperature T. The TSC-TS current spectra are integrated numerically to obtain $P(T)$ (Bucci et al. 1966):

$$\tau(T) = \frac{1}{\beta} \frac{\int_T^{T_m} J(T')\,dT'}{J(T)}, \tag{3}$$

where β is the heating rate, T_m is the temperature at which the entire charge was released, and $J(T)$ is the depolarisation current at a given temperature T. The polarisation $P(T)$ in this case is usually found as follows:

$$\beta P(T) = \int_T^{T_m} J(T')\,dT' = \int_{T_0}^{T_m} J(T')\,dT' - \int_{T_0}^{T} J(T')\,dT' = \beta P_0 - \int_{T_0}^{T} J(T')\,dT', \tag{4}$$

where P_0 is easily determined by numerically integrating the region of the entire experimental TSC-TS spectrum.

For distributed relaxation times, it is known that the BFG method gives underestimated values of the activation energy E_a (van Turnhout 1971), although with sufficiently narrow polarisation windows used in the TSC-TS method, this is not so significant and can be corrected by introducing some empirical correction (Teyssedre, Lacabanne 1995), taking into account the fact that P_0 in the case of the relaxation

 https://www.doi.org/10.33910/2687-153X-2021-2-4-157-164

time distribution is somewhat larger than in the case of a single relaxation time. Taking into account such an amendment leads to the equation:

$$\beta P(T) = \frac{\beta P_0}{1,3} - \int_{T_0}^{T} J(T')\,dT' \tag{5}$$

The modified value of *P(T)* is then used in equation (2) and, at a heating rate of several degrees per minute, gives for most polymers a relaxation time value lying in the range of $10^1 < \tau < 10^4$ c. The temperature dependence of the relaxation time is used later for the analysis of relaxation data:

$$\tau(T) = \tau_0 \exp\left(\frac{E_a}{RT}\right), \tag{6}$$

where τ_0 is the pre-exponential factor, E_a is the activation energy, and R is the universal gas constant. Unfortunately, in many cases, for example, near the glass transition temperatures of polymers, the use of equation (6) leads to sufficiently high values of E_a and unrealistic values of relaxation times (less than 10–20 s).

Another method of empirical analysis, which is usually used and can give more physically realistic parameters, at least in the case of non-cooperative relaxations at not very high temperatures, is based on the equation of activated Eyring states. In this case, this equation is used:

$$\tau(T) = \frac{h}{kT} \exp\left(\frac{\Delta H}{RT}\right) \exp\left(-\frac{\Delta S}{R}\right), \tag{7}$$

where k is Boltzmann's constant, h is Plank's constant, and ΔH, ΔS and $\Delta G = \Delta H - T\Delta S$ are the enthalpy of the activated states, entropy and free energy, respectively. It follows that the construction of a graph corresponding to equation (7) in Arrhenius coordinates $ln(1/\tau T) \sim 1/T$ allows us to calculate the enthalpy and entropy, and only then the activation energy per mole of the substance $E_a = \Delta H - T\Delta S$ and τ_0.

When interpreting the data of fractional purification, the so-called compensation law, or the "isokinetic" effect, can also be used (Ibar 1993). Compensation equation

$$\tau_0 = \tau_c \exp\left(-\frac{E_a}{RT_c}\right) \tag{8}$$

assumes the presence of a compensation temperature T_c, at which all relaxations are observed for the same time τ_c , or in other words, a linear dependence between the activation energy of "individual" relaxations and $\ln(\tau_0)$. The construction of this dependence again in the Arrhenius coordinates $\ln(\tau_0) \sim E_a/R$ makes it possible to determine both the compensation temperature T_c, and τ_c.

Substitution (8) in (6)gives

$$\tau(T) = \tau_c \exp\left(\frac{E_a}{R}\left(\frac{1}{T} - \frac{1}{T_c}\right)\right), \tag{9}$$

which in its form is in principle similar to the Eyring equation (7) and allows us to find all the parameters of the relaxation process.

Results

Figure 3 shows the results of temperature dependence of depolarisation currents for PET films exposed to UV light, obtained by TSC method. The graphs show characteristic current maximums located in the glass transition region.

Using the Tikhonov's regularising algorithms method, the parameters of electrically active defects were calculated. The results are presented in Table 1.

It can be noticed that the values of the activation energy and the frequency factor are abnormally high. As mentioned above, this calculation method does not take into account the change in entropy, which leads to an error.

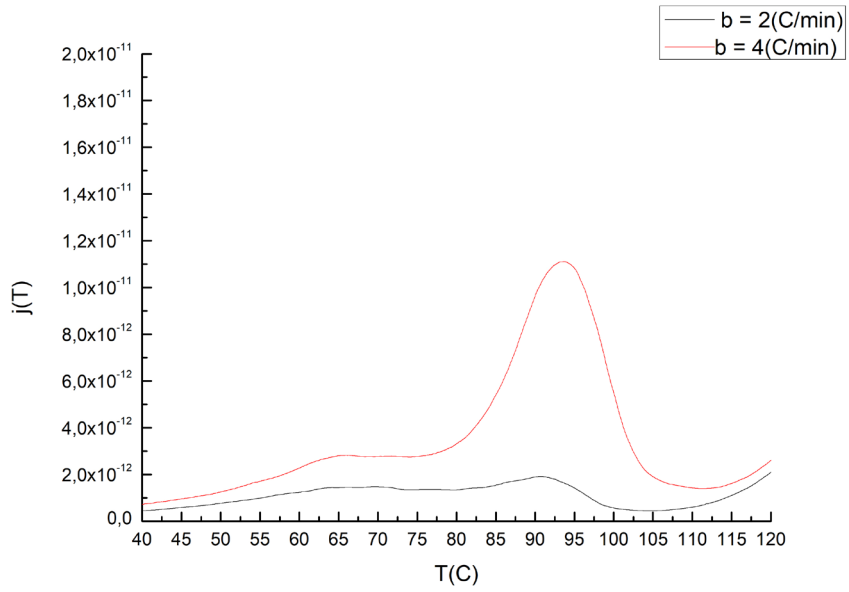

Fig. 3. Depolarisation currents for PET films. (2 and 7 indicate the heating rate in °C / min, respectively)

Table 1. Results obtained by Tikhonov's regularising algorithms method

Heating Rate, °C / min	T_m(°C)	log (τ_0)	E_a(eV)
2	90.6	–54	3.9
4	92.6		

Fig. 4 shows the results of temperature dependence of depolarisation currents for PET films exposed by UV light, obtained by TSC-TS method. The relaxation parameters were calculated using the methods described above. The values obtained using equation (6) are presented in Table 2. The values obtained using equation (7) are presented in Table 3. An illustration of the compensation law for PET films is the graphs of BFG-relaxations constructed in Arrhenius coordinates (Fig. 5).

It is notable the slope of individual lines obtained at different polarisation temperatures increases as they approach the glass transition temperature, and their extrapolation falls into one point in the frequency-temperature space, which is determined by two compensation parameters: τ_c and T_c (their values are shown on the graph). Substituting these values in (8) allows us to determine the value log (τ_0) = –13,3 which agrees fairly well with the data in Table 3.

Conclusion

In this paper, methods for obtaining parameters of electrically active defects by processing the results of TSC and TSC-TS measurements were investigated. A comparison of the obtained data showed that when processing the results of thermal activation spectroscopy of relaxation processes in the polymer glass transition region, the use of the Eyring equation or the compensation law proves the most accurate.

The value of the activation energy determined with their help for the PET exposed to UV rays turned out to be 1.07 eV, and the value of effective frequency factor $\omega = 1/\tau_0 = 5 \times 10^{10}$ c^{-1}.

Conflict of interest

The authors declare that there is no conflict of interest, either existing or potential.

https://www.doi.org/10.33910/2687-153X-2021-2-4-157-164

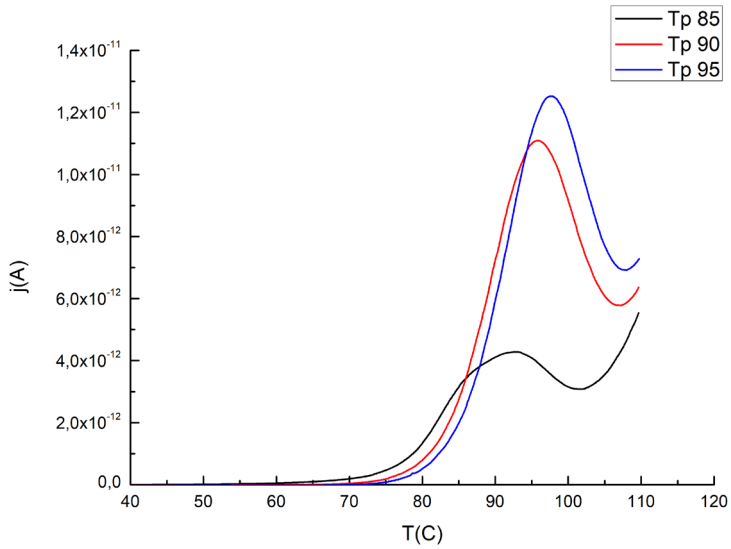

Fig. 4. Depolarisation currents for PET films (TSC-TS) (95, 90 and 85 indicate the polarisation temperatures in °C / min, respectively)

Table 2. Results obtained using equation (6)

T_p(°C)	T_m(°C)	log(τ_0)	E_a (eV)
85	92.8	–21.5	1.68
90	95.9	–30.7	2.35
95	97.7	–30.2	2.33

Table 3. Results obtained using equation (7)

T_p(°C)	Tm(°C)	ΔH (kcal/mol)	ΔS (cal/K)	E_a (eV)	log(τ_0)
85	92.8	38.06	37.46	1.07	–6.6
90	95.9	53.54	79.25	1.08	–13.4
95	97.7	53.04	77.19	1.07	–12.1

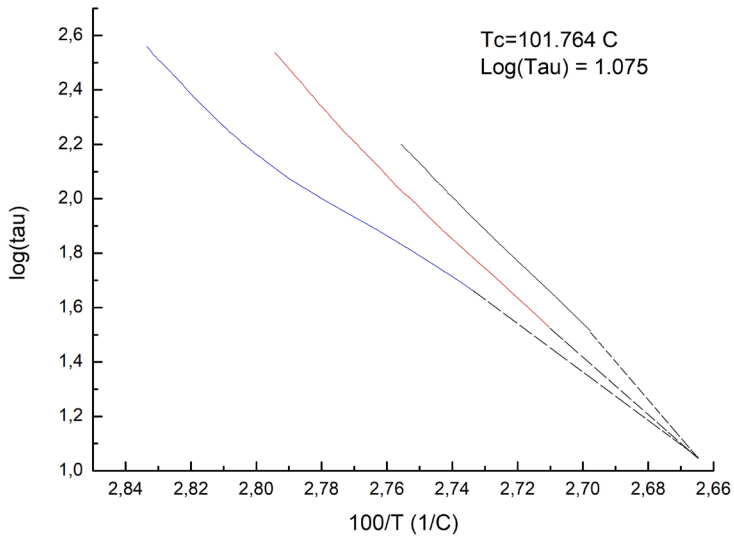

Fig. 5. An illustration of the compensation law for PET films

References

Bucci, C., Fieschi, R., Guidi, G. (1966) Ionic thermocurrents in dielectrics. *Physical Review*, 148 (2), article 816. https://doi.org/10.1103/PhysRev.148.816 (In English)

Gorohovatskij, Yu. A., Temnov, D. E. (2007) Termostimulirovannaya relaksatsiya poverkhnostnogo potentsiala i termostimulirovannye toki korotkogo zamykaniya v predvaritel'no zaryazhennom dielektrike [Thermally stimulated relaxation of surface potential and thermally stimulated short circuit currents in the charged dielectric]. *Izvestia Rossijskogo gosudarstvennogo pedagogicheskogo universiteta im. A. I. Gertsena — Izvestia: Herzen University Journal of Humanities & Sciences*, 8 (38), 24–33. (In Russian)

Ibar, J. P. (1993) *Fundamentals of thermal stimulated current and relaxation map analysis*. New Canaan: SLP Press, 667 p. (In English)

Shabanova, N., Gorokhovatsky, Y., Karulina, E. (2020) Thermally stimulated short-circuit current method and features of analyzing methods on the example of EO-polymers based on PMMA-MAA and porous PET films. In: *AIP Conference Proceedings. Vol. 2308. No. 1*. S. l.: AIP Publishing LLC, article 030011. https://doi.org/10.1063/5.0033691 (In English)

Teyssedre, G., Lacabanne, C. (1995) Some considerations about the analysis of thermostimulated depolarization peaks. *Journal of Physics D: Applied Physics*, 28 (7), article 1478. https://doi.org/10.1088/0022-3727/28/7/029 (In English)

Van Turnhout, J. (1971) Thermally stimulated discharge of polymer electrets. *Polymer Journal*, 2 (2), 173–191. https://doi.org/10.1295/polymj.2.173 (In English)

Physics of Semiconductors.
Semiconductor Physics

UDC 621.315.592+538.9 https://www.doi.org/10.33910/2687-153X-2021-2-4-165-171

The valence zone structure in $PbSb_2Te_4$ and anisotropy of hole relaxation time

S. A. Nemov✉[1], V. D. Andreeva[1], V. Volkhin[2], V. Yu. Proklova[3], Yu. V. Ulashkevich[4]

[1] Peter the Great St. Petersburg Polytechnic University, 29 Polytechnicheskaya Str., Saint Petersburg 195251, Russia
[2] Saint Petersburg Electrotechnical University "LETI", 5 Professora Popova Str., Saint Petersburg 197376, Russia
[3] Transbaikal State University, 30 Aleksandro-Zavodskaya Str., Chita 672039, Russia
[4] Ioffe Institute, 26 Polytechnicheskaya Str., Saint Petersburg 194021, Russia

Authors
Sergey A. Nemov, ORCID: 0000-0001-7673-6899, e-mail: nemov_s@mail.ru
Valentina D. Andreeva, ORCID: 0000-0001-6085-4153, e-mail: avd2007@bk.ru
Vitaliy Volkhin, e-mail: vitaly10121998@gmail.com
Viktoriya Yu. Proklova, e-mail: PVictoria78@mail.ru
Yuri V. Ulashkevich

For citation: Nemov, S. A., Andreeva, V. D., Volkhin, V., Proklova, V. Yu., Ulashkevich, Yu. V. (2021) The valence zone structure in $PbSb_2Te_4$ and anisotropy of hole relaxation time. *Physics of Complex Systems*, 2 (4), 165–171. https://www.doi.org/10.33910/2687-153X-2021-2-4-165-171

Received 7 September 2021; reviewed 21 September 2021; accepted 21 September 2021.

Funding: The study did not receive any external funding.

Abstract. The article analyses the existing set of data on the temperature dependences of the main kinetic coefficients and the IR-reflection spectra R(ν) of the $PbSb_2Te_4$ crystals. The form of the Fermi surface is discussed. The anisotropy of holes' effective mass and relaxation time is estimated. The complex structure of the valence zone is confirmed, the values of these parameters are refined.
Complex X-ray studies of the structure and composition of $PbSb_2Te_4$ samples gave the possibilities to clarify the real crystal structure and explain the number of features in the IR-reflection spectra.

Keywords: crystal $PbSb_2Te_4$, semiconductor, transport properties, temperature, band structure, Fermi surface, IR-reflection, X-ray investigations.

Introduction

$PbSb_2Te_4$ crystals belong to the class of layered tetradymite-like chalcogenides having a rhombohedral symmetry. The typical examples of this class are well-studied thermoelectric materials: bismuth (Bi_2Te_3) and antimony (Sb_2Te_3) tellurids (Goltsman et al. 1972).

$PbSb_2Te_4$ crystals usually grow with a significant deviation from the stoichiometric composition. The main feature of the samples is a large number of different electrically active point defects leading to the hole conductivity (Shelimova et al. 2004; 2007). Most of the studied crystals according to the data from the Hall effect have high concentrations of holes $p \sim 1 \times 10^{20}$ cm^{-3} (Zhitinskaya et al. 2008).

The strong anisotropy of the crystal lattice determines the anisotropy in the physical properties that are described by the tensors. In particular, the electrical conductivity and the Seebeck effect are described by the second rank tensors σ_{ik} and S_{ik}, respectively, which have two independent components along the inversion-rotary axis 3 (σ_{33} and S_{33}) and in the plane cleavage of crystals (σ_{11} and S_{11}). The Hall and Nernst-Ettingshausen effects are characterized by the third rank tensors (R_{ikl} and Q_{ikl} coefficients, respectively).

In (Nemov et al. 2013; 2014; Shelimova et al. 2007; Zhitinskaya et al. 2008), the electrophysical properties of $PbSb_2Te_4$ crystals were studied. $PbSb_2Te_4$ optical properties were not studied well. Only reflection spectra were measured (Nemov et al. 2016) and their anisotropy (Nemov et al. 2020).

The greatest anisotropy of the electrophysical properties of $PbSb_2Te_4$ crystals detected among the layered thermoelectricity of the anisotropy of $PbSb_2Te_4$ crystals (lead-antimony telluride) (Shelimova et al. 2007) is very interesting for the scientific research and from the point of view of the possible practical applications. In particular, the crystals have a significant anisotropy of the thermopower coefficients $\Delta S = S_{33} - S_{11}$ reaching 75 μV/K at room temperature.

Crystals

The studied $PbSb_2Te_4$ crystals were synthesized at the Baikov Institute of Metallurgy and Material Science, Russian Academy of Sciences. Their physical, chemical and electrophysical properties were studied in (Shelimova et al. 2004; 2007).

The $PbSb_2Te_4$ crystal lattice has rhombohedral symmetry. The crystals have a layered structure, which is based on the seven-layer packets of the atomic planes TeSbTePbTeSbTe. Those packets orderly alternate in the direction of the inversion-rotary axis of the third order $\bar{3}$.

Usually, the hexagonal elementary cell, containing 3 seven-layer packages is used. It has the following parameters: a = 0.4350 nm and c = 4.1712 nm, spatial symmetry $R\bar{3}m$ (Shelimova et al. 2004; 2007).

The chemical bond between atoms inside the seven-layer packages is ion-covalent, and between the edge tellurium atoms (Te-Te)—weak van der Waals forces.

We studied 4 $PbSb_2Te_4$ monocrystals with rather large geometric dimensions of 4 × 4 × 20 mm, including along the $\bar{3}$ axis.

Radiographs were got with the help of Bruker D8 Advance diffractometer, in monochromated $Cu_{k\alpha}$-radiation at the bundle width of 15 mm, with the divergence of 1 degree, which ensured a wide coverage of the surface.

We studied $PbSb_2Te_4$ samples in the direction of the inversion-rotary axis corresponding to the perpendicular direction of the cleavage plane in the monocrystal, and $PbSb_2Te_4$ and $PbSb_2Te_4$:Cu doped with copper (up to 0.1%) in the direction of the cleavage plane.

All studied crystals have the rhombohedral symmetry and structural parameters close to their values in (Shelimova et al. 2004; 2007). However, our results suggest that in $PbSb_2Te_4$ crystals there are two structures close in parameters with the symmetry $R\bar{3}m$ and R32, and $R\bar{3}m$ phase dominates. Figure 1 shows our results.

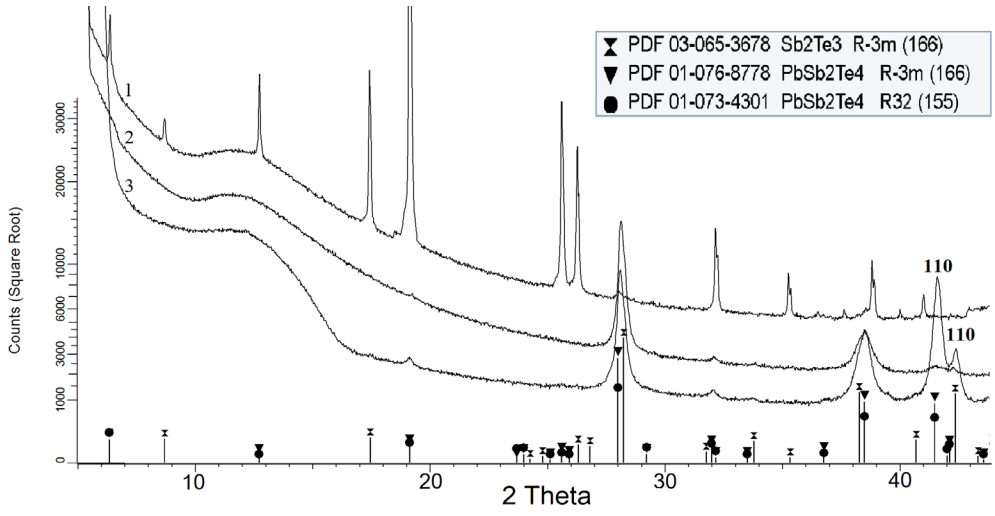

Fig. 1. Radiographs of the $PbSb_2Te_4$:Cu sample from the chip surface (1); the same (2) and the sample without copper (3) in the perpendicular C3 axis direction

The strong effect of preferential orientation of crystals in the direction 001 plane of the cleavage is visible on radiographs.

According to the calculation by Rietveld, it has been found that the content of the phase R32 with the lattice parameters a = 0.435 nm, c = 4.171 nm does not exceed 2.5–3 wt.% in samples with Cu, and less

 https://www.doi.org/10.33910/2687-153X-2021-2-4-165-171

than 1% in the sample without Cu. The amount of Sb_2Te_3 with the structure $R\bar{3}m$ in all the samples is at the level of several percent. Copper atoms having minimal dimensions (0.071 nm against 0.090 nm for Pb and Sb, and 0.111 nm for Te) during the doping of the monocrystal are embedded in the form of ions mostly between the cleavage planes. This leads to local microdeformations of the crystal lattice $R\bar{3}m$ in the perpendicular direction to the trigonal axis $C_{3,}$ as evidenced by significant, up to almost complete disappearance on the radiograph, broadening lines 110 (curves 2 and 3, 2Θ = 40–43°, Fig. 1). Relative microdeformations in these directions are 0.27% and 0.35% in five-layer Sb_2Te_3 and seven-layer $PbSb_2Te_4$ structures, respectively. The ratio *c/a* decreases from 7.15 to 7.12 for Sb_2Te_3 and from 9.62 to 9.57 for $PbSb_2Te_4$, which also indicates a less strong effect of copper atoms to change the parameter c than a (the introduction of Cu atoms into interlayer spaces of singlets has a relatively smaller effect on the dimensional characteristics of the crystalline cell than their location in more packed planes perpendicular to the C_3 axes).

Energy spectrum of holes

This section summarizes the results of transfer phenomena studies (Nemov et al. 2013; 2014; Shelimova et al. 2007; Zhitinskaya et al. 2008); the energy spectrum of holes and the parameters of current carriers are clarified.

Additional measurements of the kinetic coefficients on $PbSb_2Te_4$ crystals with the same composition as in the works (Nemov et al. 2013; 2014; Shelimova et al. 2004; 2007; Zhitinskaya et al. 2008) showed that they have similar magnitudes and temperature dependencies. So, let us go directly to the discussion of the results.

In the works (Nemov et al. 2013; 2014; Shelimova et al. 2007; Zhitinskaya et al. 2008), the valence zone structure of $PbSb_2Te_4$ and the scattering mechanisms were studied by measuring the temperature dependences of four kinetic coefficients: electrical conductivity (σ), Hall coefficients (R), thermopower (S) and transverse effect of Firstly, at the temperatures T = 120 K from 4 kinetic coefficients, the r_{kk} scattering parameter was determined in the *k* direction with the help of the formula:

$$\frac{Q_{ikl}}{R_{ikl}\sigma_{kk}S_{kk}} = \frac{r_{kk}-0.5}{r_{kk}+1},$$

where indices *i,k,l* denote the direction of measuring the electric field (EMF) $E_{i,}$ Hall and Nernst-Ettingshausen effects(*i*) , *k*-components of the current density j_k and the temperature gradient $\frac{\partial T}{\partial X_k}$, *l* is H_l component of the external magnetic field.

Further, from the data on the thermopower coefficient of S_{kk}, with the known r_{kk}, it is possible to determine the reduced chemical potential $\mu^* = \mu/k_0T$:

$$S_{kk}^{(T)} = \frac{k_0}{e}\frac{\pi^2}{3}\frac{k_0T}{\mu(T)}\left(r_{kk}+1\right), \quad (1)$$

where: k_0 is the Boltzmann constant, *e* is an electron charge module.

(*Q*) their anisotropy in temperature range 77–450 K.

Holes' concentration (p) in the studied crystals was determined from the greater component of Hall Tensor R_{123} at the temperature of 77 K, as adopted in the study of layered anisotropic materials properties of $A^V_2B^V_3$ (type Bi_2Te_3) (Golzman et al. 1972).

In $PbSb_2Te_{4\ c}$rystals, there is a number of features in the temperature dependences of the kinetic coefficients, in particular, both components of Hall Tensor R_{123} and R_{321} are characterized by the constant growth by 1.5–2 times at the range of 77–300 K. The ratio of the thermopower coefficient (S) to the temperature $\frac{S}{T}(T)$ strongly depends on the temperature, which should be approximately constant at the temperature range 77–450 in one zone model (Nemov et al. 2013).

So, the results of the transfer phenomena indicate the complexity of the zone structure scattering $PbSb_2Te_4$ and participating in transfer phenomena several types of charge carriers.

It should be noted that the analysis of experimental data was difficult because of almost the same high concentration of holes $\rho \approx 3.2 \times 10^{20}\,cm^{-3}$. Doping with a donor copper admixture (Shelimova et al. 2004; 2007) made it possible to reduce the concentration of holes by about 2 times to $\rho \approx 3.2 \times 10^{10}\,cm^{-3}$ at the temperatures near the liquid nitrogen temperature 77 K. Kinetic coefficients for this crystal qualitatively and quantitatively can be described in the framework of the one zone model (one variety of current carriers and a quadratic dispersion law). This circumstance, taking into account the strong degeneration of the hole gas, made it possible to determine the parameters of zone spectrum of holes in $PbSb_2Te_4$ sample with the minimum concentration of holes.

Estimates of the parameters of the zone spectrum were carried out as follows.

Firstly, at the temperatures T = 120 K from 4 kinetic coefficients, the r_{kk} scattering parameter was determined in the k direction with the help of the formula:

$$\frac{Q_{ikl}}{R_{ikl}\sigma_{kk}S_{kk}} = \frac{r_{kk}-0.5}{r_{kk}+1},$$

where indices i, k, l are denoted the direction of measuring the electric field (EMF) E_i, Hall and Nernst-Ettingshausen effects(i), k-components of the current density j_k and the temperature gradient $\frac{\partial T}{\partial X_k}$, l is H_l component of the external magnetic field.

Further, from the data on the thermopower coefficient of S_{kk}, with the known r_{kk}, it is possible to determine the reduced chemical potential $\mu^* = \mu/k_0T$:

$$S_{kk}^{(T)} = \frac{k_0}{e}\frac{\pi^2}{3}\frac{k_0T}{\mu(T)}\left(r_{kk}+1\right), \tag{2}$$

where k_0 is the Boltzmann constant and e is an electron charge module.

Knowing the value of $\mu^*(T)$ and using the formula

$$\mu(T) = \mu_0\left[1-\frac{\pi^2}{12}\left(\frac{k_0T}{\mu}\right)^2\right], \tag{3}$$

where μ_0 = (0 K), Fermi level E_F equal from the determination to the chemical potential at zero temperature $E_F = \mu_0$ was determined. It turned out to be 0.23 eV.

Then, from the formula for holes concentration

$$p = \frac{8\pi}{3h^3}\left(2m_d\right)^{3/2}\mu_0^{3/2}$$

the effective mass of the holes state density $m_d \approx 0.5\,m_0$ (m_0 is a mass of free electron) was determined.

At higher temperatures, Hall coefficient grows noticeably. In semiconductor physics this growth is traditionally associated with the redistribution of current carriers between non-equivalent extremums. So, calculations in this temperature area must be carried out with at least two varieties of free charge carriers, i. e., within a two-zone model.

Preliminary calculations in this model were performed in our work (Nemov et al. 2013), in which the calculation procedure was described in detail. In this work, numerical calculations have been performed within the system of equations for 4 coefficients (R, S, σ, Q) in a two-zone model. The following values of the model parameters were obtained:

The ratio of mobility of light and heavy holes $b \approx 4$–6, the effective mass of $m_{d_2} \approx 1\,m_0$, the energy gap between zones ΔE_v with increasing temperature decreases from the value of $\Delta E_v \approx 0.24$ eV (at $T \to 0$ K) with the approximate speed $\frac{d\Delta E_v}{dT} \approx -1\times10^{-4}\,eV/K$.

The qualitative nature of changing the $PbSb_2Te_4$ zone structure with temperature is shown in Fig. 2. It should be noted that the nature of the evaluations of heavy holes parameters is approximate because of the large number of unknown model parameters.

 https://www.doi.org/10.33910/2687-153X-2021-2-4-165-171

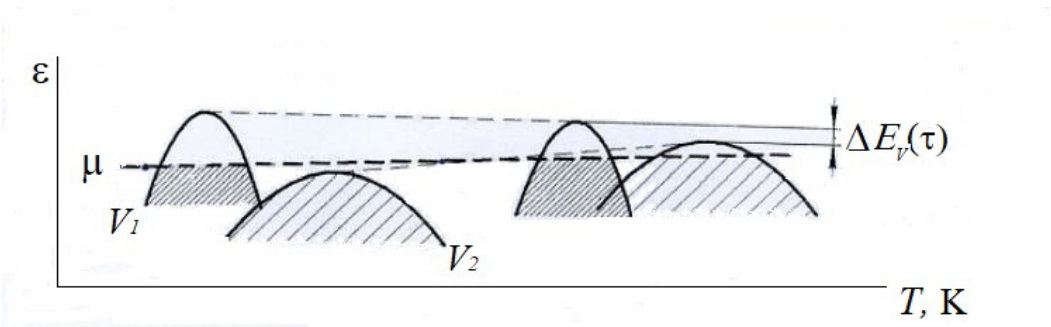

Fig. 2. Temperature displacement of zones V_1, V_2 and chemical potential μ

Fermi surface

To estimate effective mass anisotropy, it is necessary to know the type of Fermi surface.

Because of the lack of information in the scientific literature about the form of Fermi surface in *p*-$PbSb_2Te_4$ and extremum place in the Brillouin zone, let us suppose that the maximum in the valence zone is in the center, i. e., in G-point.

As the crystal lattice has symmetry on Neiman principle, Fermi surface should be the ellipsoid of rotation with the rotational axis going parallel to the symmetry axis $\bar{3}$, and effective mass tensor will have two components: longitudinal m_l (oriented along the symmetry axis) and transverse m_t (perpendicular to $\bar{3}$).

Apparently, the ellipsoids are elongated, $m_e > m_t$, since the longitudinal component of the thermopower S_e (along the C_3 axis) is larger than the transverse component S_t in the plane cleavage, perpendicular to C_3. In this case, effective mass anisotropy can be characterized by the parameter $R\bar{3}m$.

It should be noted that more complex types of Fermi surface are also possible—two ellipsoids on the symmetry axis $\bar{3}$, located symmetrically relative to G-point, as well as the combination of ellipsoids, symmetrically located relative to the axis $\bar{3}$.

Unfortunately, from the available data about kinetic coefficients (*R*, *S*, σ, *Q*) there is no possibility to determine effective mass components m_i^*, in particular from the electrical conductivity coefficient, since the formula includes the ratio of time relaxation to efficient mass:

$$\sigma = \frac{e^2 n \tau}{m^*} \cdot$$

Evaluation of effective mass anisotropy and relaxation time of holes

Taking into account the strong anisotropy of $PbSb_2Te_4$ physical properties, and also observing the significant anisotropy of the thermopower, it gives us a possibility to suggest the presence of the hole scattering anisotropy. In this case, the relaxation time will be described by the second rank tensor τ_{ik}.

In the case when both tensors of the effective mass m_{ik} and relaxation time τ_{ik} are diagonal in the same coordinate axes, the relaxation time will have two independent components—the longitudinal τ_l and τ_t. The relaxation time anisotropy will be characterized by the coefficient

$$k_\tau = \frac{\tau_e}{\tau_t} \cdot$$

Recent research of the anisotropy of $PbSb_2Te_4$ crystal reflection spectra, doped by Cu (Nemov et al. 2020) in the plasma reflection area, allows us to estimate the relaxation time anisotropy. The fact is that the experimental IR reflection spectra are well described in the framework of Drude-Lorentz model (Nemov et al. 2016; 2020) with the help of the dielectric function containing the parameter attenuation (damping) of the plasma oscillations γ, which is equal to $\gamma = 1/\tau$.

From the data (Nemov et al. 2020) we get:

$$k_\tau = \frac{\tau_e}{\tau_t} = \frac{\gamma_t}{\gamma_l} \approx \frac{44}{94} \approx 0.47 \ .$$

The received value of k_τ indicates a strong anisotropy of hole scattering compared to other semiconductors.
The frequency of plasma oscillations ω_{pl} is determined by the formula:

$$\omega_{pl}^2 = \frac{4\pi pl^2}{\varepsilon_\infty m^*},$$

where ε_∞ is a high-frequency dielectric constant.

That is why the ratio of squares of the frequency of plasma oscillations at two orientations of light wave electrical vector $\vec{E}$ along the axis $\overline{3}$ and the plane cleavage make it possible to evaluate the anisotropy coefficient of the effective conductivity mass of k_m:

$$k_m = \left(\frac{\omega_t}{\omega_l}\right)^2_{pl} \approx \left(\frac{0.52}{0.40}\right)^2 = 1.7 \ .$$

The received value confirms the elongated form of Fermi surface along the symmetry axis 3.
The ratio of conductors in the chip plane σ_t to the conductivity σ_l along the axis 3 is:

$$\frac{\sigma_t}{\sigma_l} = \frac{\tau_t}{\tau_l} \times \frac{m_l}{m_\tau} = \frac{k_l}{k} \cdot \qquad (3)$$

Substituting certain values of the anisotropy coefficients k_m and k_τ will get:

$$\frac{\sigma_t}{\sigma_l} \approx \frac{1.7}{0.47} = 3.6 \ ,$$

that is satisfactorily conforms with the data of electrical measuring.

As it was mentioned earlier, the studied crystals are not perfect. There are inclusions of the second phase of different composition and crystal lattice distortion. This circumstance explains some features of $PbSb_2Te_4$ crystal reflection spectra, that was impossible to describe with the help of the complex dielectric function ε(ν) within the framework of Drude-Lorenz models. These include the existence of the inflection point on the dependence $R(\nu)$ in the edge of plasma reflection area and the second small minimum in the area of 2300 cm^{-1} (see Fig. 3).

Conclusion

So, as a result of X-ray studies of $PbSb_2Te_4$ crystals and the analysis of the previously obtained experimental data on kinetic phenomena and IR reflections, the clarified valence zone structure and its parameters (effective weights of light and heavy holes, the temperature dependence of the energy gap between $\Delta E_V(T)$ zones) were clarified.

We have also made the estimates of the anisotropy of effective mass of holes and relaxation time, indicating their strong anisotropy.

Conflict of Interest

The authors declare that there is no conflict of interest, either existing or potential.

 https://www.doi.org/10.33910/2687-153X-2021-2-4-165-171

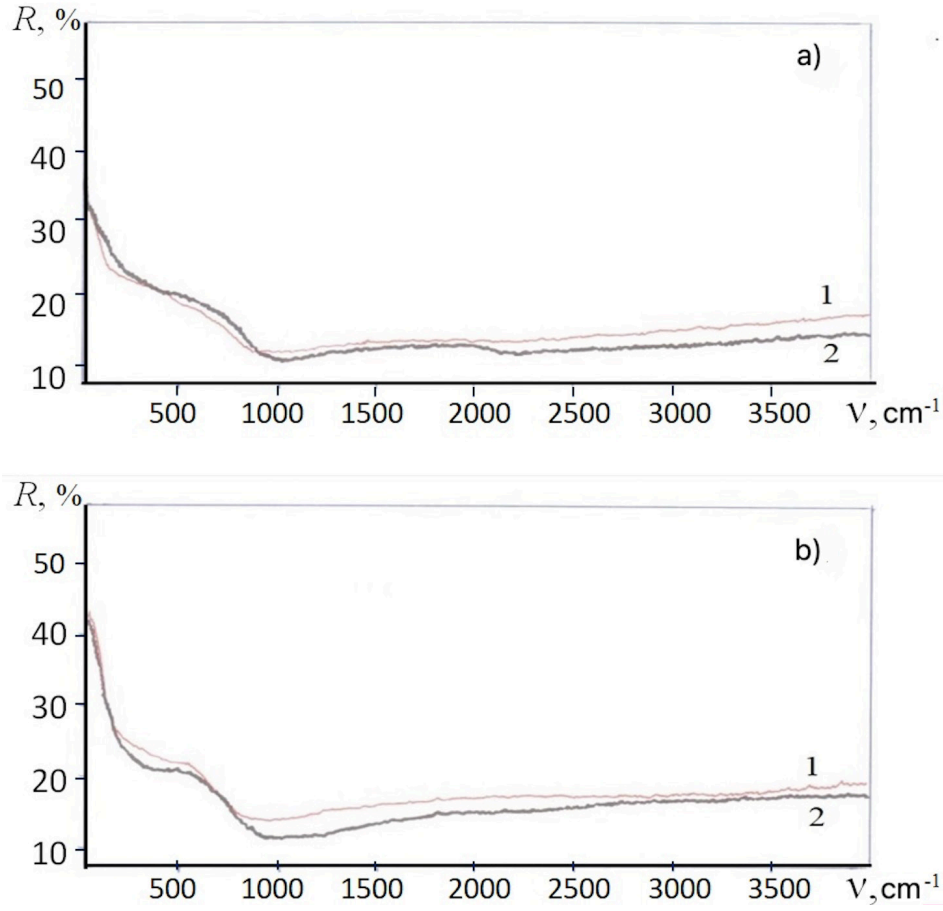

Fig. 3. Reflection spectra from the crystal chip $PbSb_2Te_4$ (a) and $PbSb_2Te_4$:Cu (*b*): 1 – T = 300 K; 2 – T = 77 K

References

Goltsman, B. M., Kudinov, V. A., Smirnov, I. A. (1972) *Poluprovodnikovye termoelektricheskie materialy na osnove Bi_2Te_3 [Semiconductor thermoelectric materials based on Bi_2Te_3]*. Moscow: Nauka Publ., 320 p. (In Russian)

Nemov, S. A., Blagikh, N. M., Dzhafarov, M. B. (2014) Effect of interband scattering on transport phenomena in p-$PbSb_2Te_4$. *Semiconductors*, 48 (8), 999–1005. https://doi.org/10.1134/S1063782614080193 (In English)

Nemov, S. A., Blagikh, N. M., Shelimova, L. E. (2013) Features of the energy spectrum and hole-scattering mechanisms in $PbSb_2Te_4$. *Semiconductors*, 47 (1), 16–21. https://doi.org/10.1134/S106378261301017X (In English)

Nemov, S. A., Ulashkevich, Yu. V., Pogumirsky, M. V., Stepanova, O. S. (2020) Reflection from the Side Face of a $PbSb_2Te_4$ Crystal. *Semiconductors*, 54 (3), 282–284. https://doi.org/10.1134/S1063782620030161 (In English)

Nemov, S. A., Ulashkevich, Yu. V., Povolotskii, A. V., Khlamov, I. I. (2016) Reflectance of a $PbSb_2Te_4$ crystal in a wide spectral range. *Semiconductors*, 50 (10), 1322–1326. https://doi.org/10.1134/S1063782616100183 (In English)

Shelimova, L. E., Karpinskii, O. G., Svechnikova, T. E. et al. (2004) Synthesis and structure of layered compounds in the PbTe–Bi_2Te_3 and PbTe–Sb_2Te_3 systems. *Inorganic Materials*, 40 (12), 1264–1270. https://doi.org/10.1007/s10789-005-0007-2 (In English)

Shelimova, L. E., Svechnikova, T. E., Konstantinov, P. P. et al. (2007) Anisotropic thermoelectric properties of the layered compounds $PbSb_2Te_4$ and $PbBi_4Te_7$. *Inorganic Materials*, 43 (2), 125–131. https://doi.org/10.1134/S0020168507020057 (In English)

Zhitinskaya, M. K., Nemov, S. A., Shelimova, L. E. et al. (2008) Thermopower anisotropy in the layered compound $PbSb_2Te_4$. *Physics of the Solid State*, 50 (1), 6–8. https://doi.org/10.1134/S1063783408010022 (In English)

Physics of Semiconductors.
Semiconductor Physics

UDC 621.3

https://www.doi.org/10.33910/2687-153X-2021-2-4-172-179

Investigation of the properties of zinc oxide based heterostructures

A. R. Semenov✉[1], T. A. Kholomina[1], V. G. Litvinov[1], A. V. Ermachikhin[1]

[1] Ryazan State Radio Engineering University named after V. F. Utkin, 59/1 Gagarina Str., Ryazan 390005, Russia

Authors

Andrey R. Semenov, ORCID: 0000-0003-2780-5661, e-mail: sem-a-sem@mail.ru

Tatiana A. Kholomina, ORCID: 0000-0003-3902-618X, e-mail: marta.tap@yandex.ru

Vladimir G. Litvinov, ORCID: 0000-0001-6122-8525, e-mail: vglit@yandex.ru

Alexander V. Ermachikhin, ORCID: 0000-0002-3808-9691, e-mail: al.erm@mail.ru

For citation: Semenov, A. R., Kholomina, T. A., Litvinov, V. G., Ermachikhin, A. V. (2021) Investigation of the properties of zinc oxide based heterostructures. *Physics of Complex Systems*, 2 (4), 172–179. https://www.doi.org/10.33910/2687-153X-2021-2-4-172-179

Received 21 September 2021; reviewed 8 October 2021; accepted 8 October 2021.

Funding: The research was supported by the Ministry of Science and Higher Education of the Russian Federation as part of a state task (FSSN-2020-0003).

Abstract. The paper presents the results of an experimental study of the electric properties of ZnO-based polycrystalline heterosructures. C-V-characteristics of In/ZnO/n-Si/Al and Au/ZnO/n-Si/Al heterostructures were modeled. Influence of upper contacts material and annealing technology on structure characteristics was investigated. Surface states influence according to applied theoretical model was analyzed. Empirical dependence of the surface potential in silicon on the voltage applied on the structure was derived.

Keywords: surface states, heterostructures, ZnO, C-V-characteristics, I-V-characteristics.

Introduction

In recent years, many scientific studies have been devoted to the study of the properties of zinc oxide. Zinc compounds are widely distributed in nature, therefore, zinc oxide is of interest as a straight-band semiconductor with a large (3.36 eV) band gap. The unalloyed material has an electronic type of conductivity in combination with good optical properties and resistance to radiation (Pintilie, Pintilie 2001). ZnO is a promising material for the production of transparent conductors in solar cells, LEDs, laser diodes, and UV photodiodes. Due to the possibility of obtaining structures with high electronic mobility, the material can be used in high-speed UV radiation sensors (Kaidashev et al. 2003).

The purpose of this work is to study the phenomena of charge transfer in semiconductor heterostructures under the action of an electric field for the development of ideas about the features of physical phenomena in microcrystalline zinc oxide films.

Samples and investigation methods

In this work, we analyzed and compared the parameters of semiconductor heterostructures of two types: zinc oxide films grown on an n+ silicon substrate with non-rectifying In contacts and rectifying Au contacts deposited on their surface (Fig. 1). The structures were annealed in argon and oxygen gases at a temperature of 600 °C. Annealing the samples of group 1 was carried out in an Ar environment, and for groups 2–4 in an oxygen atmosphere. The indium contacts were in the form of a square with a side

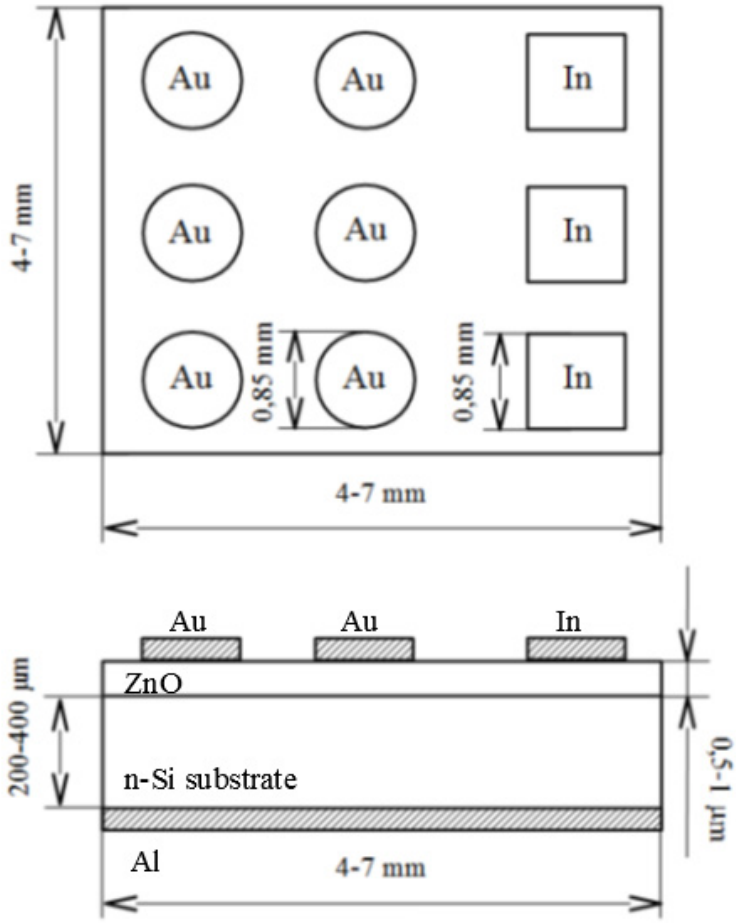

Fig. 1. Sample structure

of 0.85 mm, and the gold contacts were in the form of a circle of the same diameter. Ohmic aluminum contacts are deposited on the silicon substrate on the reverse side of the plate.

The properties of the samples were investigated by the methods of current-voltage (I-V) and capacitance-voltage (C-V) characteristics. The I-V and C-V characteristics were measured using an Agilent E4980A RLC meter.

Experimental results

The I–V characteristics of the Au/ZnO contacts were asymmetric, typical of diode structures. For the samples of group 1, an electrical breakdown was recorded at a reverse bias voltage of more than 4.7 V, in connection with which the I–V characteristics of sample groups 1–4 were further measured in the range from –3.5 to 3.5 V (Fig. 2).

The samples of group 1 showed the most pronounced rectifying I-V characteristic with a threshold voltage of about 1.8 V. For the samples of groups 2 and 3, the forward threshold voltage was about 2.1 V. At the same time, for the samples from group 4, the I–V characteristic in the test range was almost linear.

The I–V characteristics of the structures under study, obtained on ohmic In contacts, are shown in Fig. 3. The I–V characteristics were linear and symmetric. The resistivity of the ZnO layer was estimated from the linear part of the current-voltage characteristics, which turned out to be no less than 10^5 Ohm·cm for all the samples, which made it possible to consider ZnO as a dielectric (Litvinov et al. 2018). The resistances of thin layers of ZnO are calculated and are approximately equal to 0.97 MOhm for group 1; 0.40 MOhm for group 2; 1.43 MOhm for group 3 and 1.19 MOhm for group 4.

Annealing the samples in an argon atmosphere (group 1) practically does not lead to a change in the oxygen content in ZnO. It can be assumed that for the samples with a smaller thickness of group 3, the effect of the annealing atmosphere turned out to be more significant (Gromov et al. 2013). Annealing

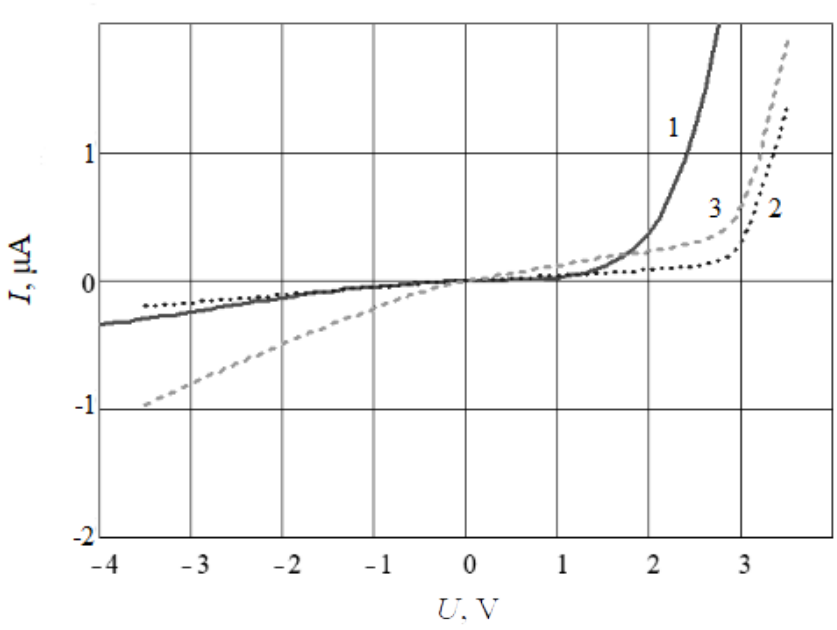

Fig. 2. I-V characteristics of barrier Au contacts for the samples of batches 1–3

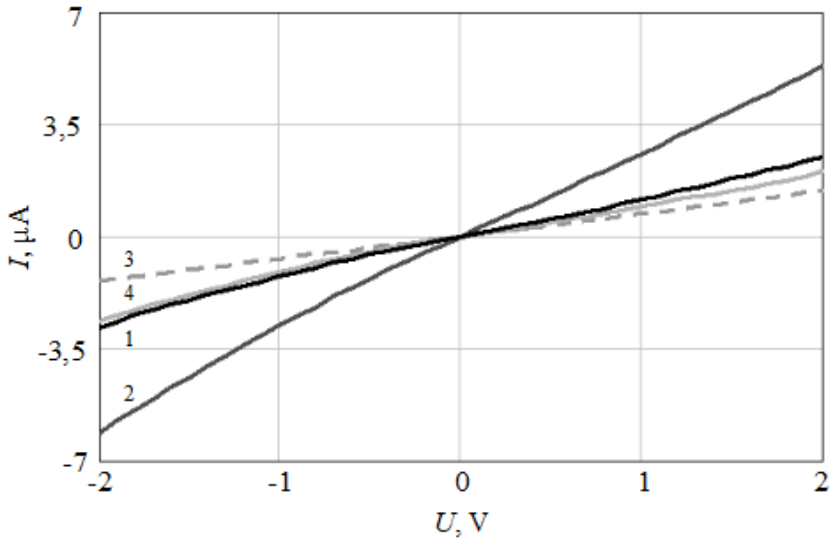

Fig. 3. I-V characteristics of In/ZnO/n-Si/Al contacts of the samples annealed in oxygen (1, 2, 3) and argon (4)

in oxygen led to a decrease in the resistance of the structure and a weak nonlinearity of the I–V characteristic. Presumably, this difference is caused by the presence of hydrogen atoms in the interstices of the crystal lattice of ZnO, which play the role of shallow donors (Ellmer et al. 2008).

Annealing is likely to result in the adsorption of oxygen atoms and the "healing" of oxygen defects—the incorporation of oxygen atoms into the ZnO crystal lattice and their bonding with zinc atoms Zn+ (Gromov et al. 2013). Zinc atoms Zn+ are located in interstices or in the lattice sites, but are not associated with oxygen atoms. The resistance of the sample of group 4 is higher than the resistance of the sample of group 1, which allows us to conclude that the annealing was carried out in a humid oxygen environment. In oxygen, some amount could contain residual gases, the atoms of which are donors. Sample group 2 had the lowest resistance, which indicates a large number of impurity donor atoms of residual gases and hydrogen.

The analytical relations, in accordance with which the calculation of the values of the electrophysical parameters of thin ZnO films were made, are given in (Muller et al. 2003; Oreshkin 1977).

 https://www.doi.org/10.33910/2687-153X-2021-2-4-172-179

The concentration of donors N_d in highly doped n-type silicon, according to the sample manufacturers, was about 10^{18} cm^{-3}. Our calculations showed that the Fermi level in ZnO for all groups of samples turned out to be above the middle of the band gap, which corresponds to the n-type conductivity.

The experimental C-V characteristics of the investigated heterostructures are, in general, similar to the characteristics of MIS structures. Small differences were observed in the region of enrichment of the ZnO/n-Si interface with charge carriers. Therefore, to analyze the C-V characteristics of heterostructures with ZnO films, in this work, we applied the theoretical model of the MIS structure, since the high-resistance layers of wide-gap zinc oxide act as a dielectric.

The approximation of the experimental C-V characteristics was carried out in the areas of weak inversion, depletion and accumulation of low-frequency C-V characteristics of the ideal MIS structure. The constructed model curves were the dependences of the capacitance on the surface potential ψ_s or the potential on the depleted layer of the semiconductor substrate (Sze 1981).

The capacitance of the structure is presented as a series connection of the capacitance of the dielectric and the differential capacitance of the semiconductor:

$$C_D = -\frac{\varepsilon_S \varepsilon_0}{\sqrt{2} L_D} \frac{1 - e^{\beta\psi_S} + \left(p_{n_0} / n_{n_0} \right) \left(1 + e^{-\beta\psi_S} \right)}{F\left(\beta\psi_S, p_{n_0} / n_{n_0} \right)}, \tag{1}$$

$$C_{Theory}\left(\psi_S\right) = \left(\frac{1}{C_{Ei}} + \frac{1}{C_D\left(\psi_S\right)} \right)^{-1}. \tag{2}$$

where $C_D(\psi_s)$—effective differential capacitance of depleted semiconductor layer, C_{Ei}—effective dielectric capacitance, $C_{theory}(\psi_s)$—effective theoretical capacitance of MOS structure, ε_s—relative permittivity of semiconductor, ε_0—dielectric constant, L_D—electron Debye length, β—coefficient $\beta = q/kT$, q—elementary charge, k—Boltzmann constant, T—temperature, n_0 and p_0—equilibrium concentrations of electrons and holes respectively. The function $F(\psi_s)$ is defined as

$$F(\psi_S) = \sqrt{\left(-\exp(\beta\psi_S) + \beta\psi_S + 1\right) - \frac{n_0}{p_0}\left(\exp(-\beta\psi_S) + \beta\psi_S + 1\right)}. \tag{3}$$

Flat band capacity of the selected sample was found as the capacity at the surface potential $\psi_s = 0$. In that case effective differential capacitance is defined as

$$C_D\left(0\right) = \frac{\varepsilon_S \varepsilon_0}{L_D}. \tag{4}$$

Since zero surface potential on ideal MIS structure is equal to zero voltage on the investigated structure, then the value of the fixed charge is determined by the shift of the experimental dependence on the stress axis. Surface charge is generally a sum of several components (Sze 1981):

- the charge captured by surface traps;
- fixed oxide charge near the interface of semiconductor and dielectric;
- trapped oxide charge generated by x-ray irradiation of structures or injection of hot electrons into the dielectric;
- the charge of mobile ions.

In the model we use, a fixed oxide charge Q_f is considered to be prevailing because other components of the surface charge can be neglected: the samples were not exposed to radiation, the charge captured by surface traps is considered as nonexistent when $\psi_s = 0$ and under existing fabrication conditions the presence of mobile ions is unlikely.

Fixed charge in the real MIS structure was defined as (Sze 1981):

$$Q_f = C_{Ei} \times (\varphi_{ms} - \Delta U_{FB}). \quad (5)$$

The next stage of the analysis was to determine the density of surface states at the ZnO-Si interface. The calculation of the density of surface states was carried out by the high-frequency capacitive method based on the concepts described by Terman (Semenov et al. 2018). It was assumed that the change in the charge on the structure in the state of flat bands is the same for small changes in the voltage on the structure and the surface potential (Sze 1981).

The value of the derivative of the surface potential from the voltage $d\psi_S/dU$ is found as the ratio of the derivative of the experimental capacitance versus the voltage across the structure and the derivative of the calculated capacitance versus the surface potential of the semiconductor.

When connecting Au-substrate contacts, for example, the samples of group 2, the $d\psi_S/dU$ value in the state of flat zones was 0.28. The density of surface states D_{it} is determined by the formula (Sze 1981):

$$D_{it} = \frac{C_{Ei}}{q}\left(\left(\frac{d\psi_S}{dU}\right)^{-1} - 1\right) - \frac{C_D}{q}. \quad (6)$$

In the first approximation, the derivative $d\psi_S/dU$ was considered constant at all voltage values, therefore, $\psi_S = 0.28 \times U$.

The CV characteristics were used to calculate the spectra of the density of surface states at the ZnO/n-Si interface, from which it follows that upon annealing zinc oxide films in argon, the effective density of states of Au/ZnO/n-Si heterostructures is approximately an order of magnitude higher than upon annealing in oxygen (3.5×10^{12} and 6×10^{11} eV^{-1} cm^{-2}, respectively).

As a result of the analysis of the experimental data, the following values of the parameters of the samples were obtained, shown in Table 1.

Calculations showed that the obtained values of the concentration of charge carriers and the capacitance of the dielectric for different samples were of approximately the same order of magnitude, which agrees with the manufacturing conditions. The obtained values of the effective density of surface states are in the range characteristic of the silicon-dielectric interface.

The value of the relative permittivity, according to calculations, turned out to be below the table value ($\varepsilon_i = 9$). It can be assumed that this is caused by the inhomogeneity of the surface of the ZnO films and requires additional study.

The theoretical and experimental C-V characteristics are shown in Figure 4.

Table 1. Parameters of the investigated heterostructures

Parameter	Sample group			
	1	2	3	4
ZnO film thickness d, μm	0.71	0.84	0.62	1.2
Sample resistance R, MOhm	0.97	0.4	1.43	1.19
Sample resistivity ρ, MOhm·cm	98.7	34	165.8	71.9
Concentration of free charge carriers (electrons) in ZnO, $n_0 \times 10^8$, cm^{-3}	3.16	9.18	1.88	4.34
Effective density of states in the conduction band in silicon, N_c, cm^{-3}	$3{,}5 \times 10^{18}$			
Position of the Fermi level relative to the bottom of the conduction band $W_f - W_c$, eV	–0.6	–0.57	–0.61	–0.59
Work function $q\phi_s$, eV	4.95	4.92	4.96	4.94

 https://www.doi.org/10.33910/2687-153X-2021-2-4-172-179

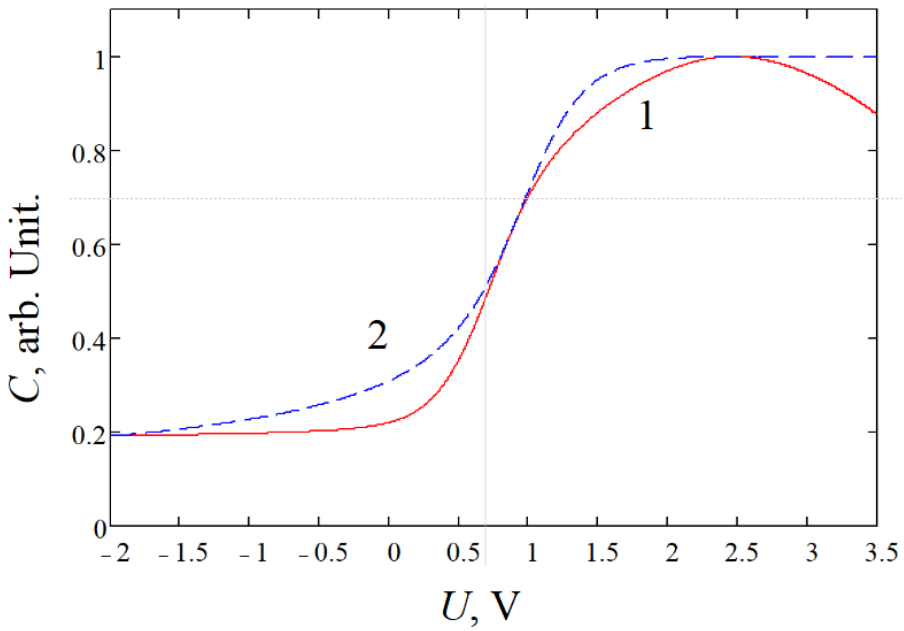

Fig. 4. Experimental C-V characteristic for the sample of group 1 measured on Au contacts at a frequency of 1 kHz (Trace 1) and modeled theoretical dependence for an ideal MIS structure at low frequencies with flat band voltage offset and the surface state density taken into account (Trace 2)

The use of the described method gives an acceptable agreement between the experimental and theoretical C-V characteristics, which is confirmed by the value of the Pearson correlation coefficient k_p = 0.9959008 (Pearson 1895). A similar approximation was carried out for all the samples when connected to rectifying (Au) and non-rectifying (In) contacts. Note that for all the samples, the model and experimental characteristics for the depletion region practically coincided.

Comparison of the measurement results was carried out for different contacts on each sample (Fig. 5).

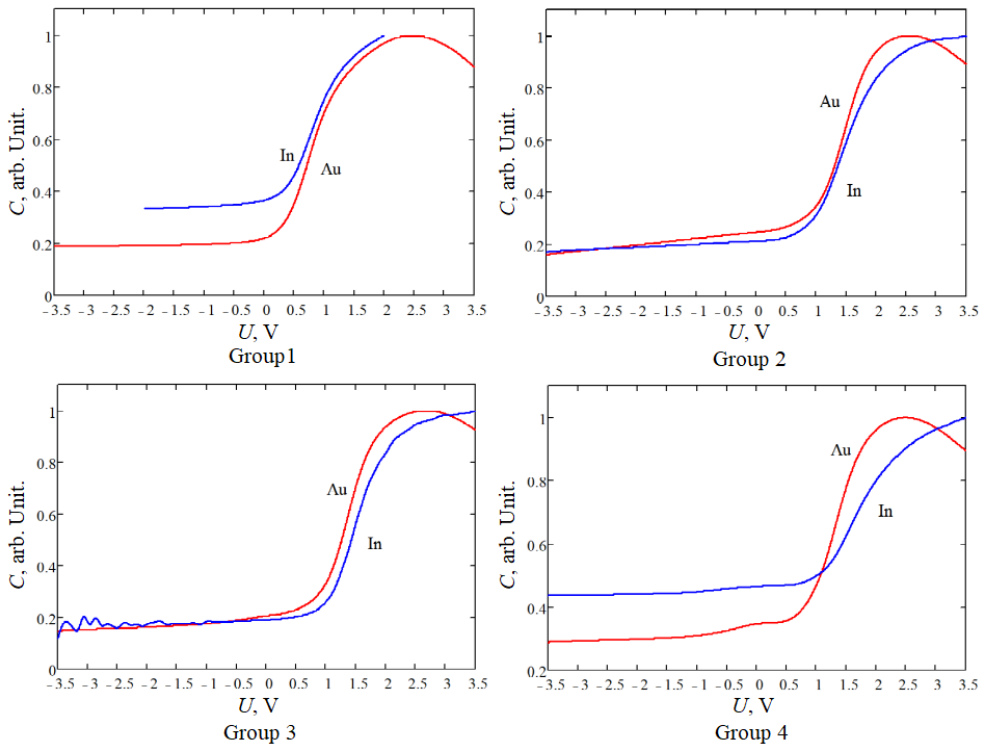

Fig. 5. Comparison of the normalized dependences of the effective capacity of the samples of a batch on the voltage for Au and In contacts

The authors of (Pearton et al. 2005) noted the presence of electron traps with energies of 0.2 and 0.3 eV at the Au-ZnO interface. Another factor affecting the capacitance characteristics is the possible inhomogeneity of the thickness of the ZnO thin film. The diffusion of metal atoms from the contacts into the bulk of ZnO is possible, which reduces the thickness of the insulating layer.

The comparison of the measurement results was carried out for different contacts on each sample. Since for each group of the samples we are talking about the same silicon substrate, the differential capacitance for each group of the samples should be the same. However, for the samples of groups 1 and 4, the differential capacities in the case of measurements at the In/ZnO/n-Si/Al and Au/ZnO/n-Si/Al contacts are different. This may be due to the nonuniform distribution of defects and traps at the ZnO/n-Si interface, charge spreading, and an increase in the effective area of the upper contact when the In/ZnO/n-Si/Al contact is connected.

The difference between the theoretically calculated and experimental values of the specific capacity of the investigated samples with Au/ZnO/n-Si/Al contacts is shown in Fig. 6.

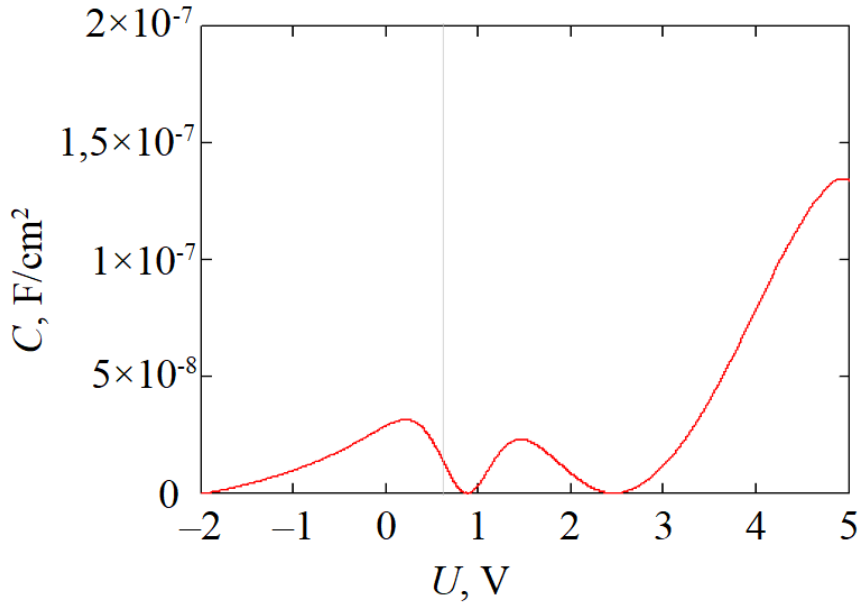

Fig. 6. The difference between the theoretically calculated and experimental value of the capacitance of the samples of batch 1 at the rectifying contacts at a frequency of 1 kHz

With an increase in the positive potential, a noticeable decrease in the ZnO capacitance is observed, possibly associated with the activation and movement of mobile ions in the dielectric film. The difference in the capacitance in the accumulation mode of the In/ZnO/n-Si/Al and Au/ZnO/n-Si/Al connections, and the type of capacitance-voltage characteristic for the rectifying contact indicated the presence of a built-in charge trapped in traps at the Au-ZnO boundary.

Conclusion

The study of current-voltage and capacitance-voltage characteristics of semiconductor heterostructures In/ZnO/n-Si/Al and Au/ZnO/n-Si/Al has been carried out.

The influence of the technology of annealing the samples based on microcrystalline ZnO and the contact material on the characteristics of the structures is investigated.

It was found that the experimental capacitance-voltage characteristics of the objects under study are, in general, similar to the characteristics of MIS structures. Based on this, it was concluded that thin ZnO films in In/ZnO/n-Si/Al and Au/ZnO/n-Si/Al heterostructures can be regarded as an analogy of the dielectric of MIS structures.

The processing of the results obtained in the Mathcad programme made it possible to obtain the value of the density of surface states, the value of the built-in surface charge, to estimate the value of the concentration of free charge carriers in the silicon substrate, and other parameters.

 https://www.doi.org/10.33910/2687-153X-2021-2-4-172-179

It was found that upon annealing zinc oxide films in argon, the effective density of states of Au/ZnO/n-Si heterostructures is approximately an order of magnitude higher than upon annealing in oxygen (3.5×10^{12} and 6×10^{11} eV^{-1} cm^{-2}, respectively).

Possible reasons for the deviation of the capacitance of the heterostructure from the theoretically calculated values are analyzed.

Conflict of Interest

The authors declare that there is no conflict of interest, either existing or potential.

Author Contributions

A. R. Semenov and A. V. Ermachikhin carried out the planning and conducting of experimental research; V. G. Litvinov and T. A. Kholomina participated in the processing and interpretation of the results; all authors participated in the discussion of the results and the formulation of conclusions.

Acknowledgements

The authors are deeply grateful to D. G. Gromov and S. P. Oleinik (NRU MIET) for the samples provided for the study. The work was carried out using the equipment of the Regional Center for Probe Microscopy for Collective Use of the Ryazan State Radio Engineering University named after V. F. Utkin (RSREU).

References

Ellmer, K., Klein, A., Rech, B. (eds.). (2008) *Transparent conductive zinc oxide. Basics and applications in thin film solar cells*. Berlin; Heidelberg: Springer Verlag, 445 p. https://doi.org/10.1007/978-3-540-73612-7 (In English)

Gromov, D. G., Koz'min, A. M., Shulyat'ev, A. S. et al. (2013) Effect of the formation conditions on the properties of ZnO:Ga thin films deposited by magnetron-assisted sputtering onto a cold substrate. *Semiconductors*, 47 (13), 1687–1691. https://doi.org/10.1134/S1063782613130083 (In English)

Kaidashev, E. M., Lorenz, M., von Wenckstern, H. et al. (2003) High electron mobility of epitaxial ZnO thin films on c-plane sapphire grown by multistep pulsed-laser deposition. *Applied Physics Letters*, 82 (22), 3901–3903. https://doi.org/10.1063/1.1578694 (In English)

Litvinov, V. G., Semenov, A. R., Kholomina, T. A. et al. (2018) Issledovanie spectra poverkhnostnykh sostoyanij na granitse razdela geterostruktury ZnO/Si [Investigation of surface spectra on ZnO/Si interface]. *Vestnik Ryazanskogo gosudarstvennogo radiotekhnicheskogo universiteta — Vestnik of Ryazan State Radio Engineering University*, 4 (66-2), 9–14. https://doi.org/10.21667/1995-4565-2018-66-4-2-9-14 (In Russian)

Muller, R. S., Chan, M., Kamins, T. I. (2003) *Device electronics for integrated circuits*. 3rd ed. New York: Wiley Publ., 528 p. (In English)

Oreshkin, P. T. (1977) *Fizika poluprovodnikov i dielektrikov [Physics of semiconductors and dielectrics]*. Moscow: Vysshaya shkola Publ., 448 p. (In Russian).

Pearson, K. (1895) Note on regression and inheritance in the case of two parents. *Proceedings of the Royal Society of London*, 58 (347–352), 240–242. https://doi.org/10.1098/rspl.1895.0041 (In English)

Pearton, S. J., Norton, D. P., Ip, K. et al. (2005) Recent progress in processing and properties of ZnO. *Progress in Materials Science*, 50 (3), 293–340. https://doi.org/10.1016/j.pmatsci.2004.04.001 (In English)

Pintilie, L., Pintilie, I. (2001) Ferroelectrics: New wide-gap materials for UV detection. *Materials Science and Engineering: B.*, 80 (1–3), 388–391. https://doi.org/10.1016/S0921-5107(00)00605-X (In English)

Semenov, A. R., Litvinov, V. G., Kholomina, T. A. et al. (2018) Investigating and modeling high frequency C-V characteristics of zinc oxide-based heterostructures. In: *7th Mediterranean Conference on Embedded Computing: (MECO–2018)*. Budva: IEEE Publ., pp. 1–4. https://doi.org/10.1109/MECO.2018.8405999 (In English)

Sze, S. M. (1981) *Physics of Semiconductor Devices*. 2nd ed. New York: Wiley Publ., 868 p. (In English)

Theoretical physics. Cosmology

UDC 524.8 https://www.doi.org/10.33910/2687-153X-2021-2-4-180-184

Forces for the particles with a zero energy in Kerr metric

A. A. Grib[1], V. D. Vertogradov[✉1,2], L. A. Shleiger[1]

[1] Herzen State Pedagogical University of Russia, 48 Moika Emb., Saint Petersburg 191186, Russia
[2] The SAO RAS, Pulkovskoe shosse 65, Saint Petersburg 196140, Russia

Authors
Andrey A. Grib, ORCID: 0000-0002-6389-991X, e-mail: andrei_grib@mail.ru
Vitalii D. Vertogradov, ORCID: 0000-0002-5096-7696, e-mail: vdvertogradov@gmail.com
Leonid A. Shleiger, e-mail: lslejger@gmail.com

For citation: Grib, A. A, Vertogradov, V. D., Shleiger, L. A. (2021) Forces for the particles with a zero energy in Kerr metric. *Physics of Complex Systems*, 2 (4), 180–184. https://www.doi.org/10.33910/2687-153X-2021-2-4-180-184

Received 21 September 2021; reviewed 28 September 2021; accepted 28 September 2021.

Funding: The work was performed within the SAO RAS state assignment in the part "Conducting Fundamental Science Research".

Abstract. The particles with negative energy might exist in the ergosphere of a rotating black hole due to collision or decay. We also know that there might be particles with zero energy in this region. In this paper we find out how the geodesic equations depend upon the energy and consider forces which act on the particles with zero energy. Also, we investigate the question how these forces for particles with zero energy differ from the ones in the case of usual positive energy *E*. We find out that the forces in the usual case are less than in the case of zero energy.

Keywords: Black hole, Kerr spacetime, ergosphere, zero energy, forces.

Introduction

In 1969, Penrose theorized an effect (Penrose 1969) which was called the Penrose process. According to this effect the particles with negative energy can exist in the ergosphere of a rotating black hole due to decay or collision. The thorough analysis of geodesics for such particles has been done in (Grib et al. 2014). Later, it was understood that there might be particles with zero energy (Grib, Pavlov 2017). This effect is possible due to the fact that the Killing vector $\frac{d}{dt}$ is spacelike in the ergosphere and the parameter E, which is the energy with regard to infinity, might be either negative or equal to zero (Vertogradov 2015). If we consider the second order geodesic equation, then we obtain Newton's second law of mechanics and it is very interesting how negative or zero energy changes the forces which act on the particle. In this paper we will consider only radial movement in the equatorial plane $\theta = \pi/2$ and forces which act on the particle with zero energy.

The paper is organized as follows. In Section 2 we will discuss some properties of the Kerr metric and obtain the geodesic equation in this spacetime. Section 3 represents the discussion of the forces which act on the particle with zero energy and their difference to usual case of positive energy. Section 4 is the conclusion.

The Kerr metric. General notes

A metric of a neutral rotating black hole is a well-known solution of the Einstein equation obtained by Kerr (Teukolsky 2015). The Kerr metric in Boyer-Lindquist coordinates has the following form (Chandrasekhar 1983; Poisson 2004; Vladimirov 2009):

$$ds^2 = -\left(1-\frac{2Mr}{\rho^2}\right)dt^2 - \frac{4Mra\sin^2\theta}{\rho^2}dt\,d\varphi + \frac{\rho^2}{\Delta}dr^2 + \rho^2 d\theta^2 + \left(r^2 + a^2 + \frac{2Mra^2\sin^2\theta}{\rho^2}\right)\sin^2\theta d\varphi^2 \tag{2.1}$$

where, $\rho^2 = r^2 + a^2\cos^2\theta$; $\Delta = r^2 - 2Mr + a^2$
M—is the mass of the black hole and a—is its rotation.

To calculate the force expression, one should know non-vanishing components of the Christoffel symbols Γ^i_{kl}. In this paper we only consider the case of the equatorial plane $= \pi/2$. In this case non-vanishing Christoffel symbols are given by:

$$\Gamma^0_{01} = \frac{Mr^2\left(a^2+r^2\right)}{r^2\left(a^2+r^2\right)\left(r^2-2Mr\right)+2Mra}$$

$$\Gamma^0_{02} = \frac{-a^2\left(a^4M + 2r^3\left(Mr-2M^2\right)+a^2\left(3Mr-2M^2\right)\right)}{2r\left(r^2\left(a^2+r^2\right)\left(r^2-2\mathrm{Mr}\right)+2Mra\right)}$$

$$\Gamma^0_{13} = \frac{-aMr^2\left(a^2+3r^2\right)}{r^2\left(a^2+r^2\right)\left(r^2-2\mathrm{Mr}\right)+2Mra}$$

$$\Gamma^1_{00} = \frac{M\Delta}{r^4}$$

$$\Gamma^1_{03} = -\frac{aM\Delta}{r^4}$$

$$\Gamma^1_{11} = \frac{a^2-Mr}{r\Delta}$$

$$\Gamma^1_{22} = -\frac{\Delta}{r}$$

$$\Gamma^1_{33} = \frac{-\Delta\left(2r-\frac{2a^2M}{r^2}\right)}{r^2}$$

$$\Gamma^2_{03} = \frac{aM\left(a^2+r^2\right)}{r^5}$$

$$\Gamma^2_{12} = \frac{1}{r}$$

$$\Gamma^3_{01} = \frac{aM}{r^2\left(a^2+r^2\right)\left(r^2-2\mathrm{Mr}\right)+2Mra}$$

$$\Gamma^3_{31} = \frac{r\left(r^3\left(r-2M\right)-a^2Mr\right)}{r^3\left(r-2M\right)\left(a^2+r^2\right)+2a^2Mr} \tag{2.2}$$

From (2.2) by using formula:

$$\frac{d^2x^i}{d\tau^2} + \Gamma^i_{kl}\frac{dx^k}{d\tau}\frac{dx^l}{d\tau} = 0 \tag{2.3}$$

one can easily write the geodesic equation. We are interested only in the radial equation. In the Kerr metric it is given by:

$$\frac{d^2r}{d\tau^2} = -\frac{M\Delta}{r^4}\left(\frac{dt}{d\tau}\right)^2 + \frac{2aM\Delta}{r^4}\frac{dt}{d\tau}\frac{d\varphi}{d\tau} + \frac{Mr-a^2}{r\Delta}\left(\frac{dr}{d\tau}\right)^2 + \frac{\Delta\left(2r-\frac{2a^2M}{r^2}\right)}{r^2}\left(\frac{d\varphi}{d\tau}\right)^2, \tag{2.4}$$

(where τ is the proper time)

In the left-hand side we have a radial acceleration. So, in the right-hand side one should have the radial component F_r of the three force divided by the mass of the test body m.

However, one should pay attention only to components $\Gamma^1_{00}\left(\frac{dt}{d\tau}\right)^2 = \frac{M\Delta}{r^4}\left(\frac{dt}{d\tau}\right)^2$ and $2\Gamma^1_{03}\frac{dt}{d\tau}\frac{d\varphi}{d\tau} = -2\frac{aM\Delta}{r^4}\frac{dt}{d\tau}\frac{d\varphi}{d\tau}$ (Landau, Lifshitz 1976).

The components $\Gamma^1_{11}\left(\frac{dr}{d\tau}\right)^2$, $\Gamma^1_{33}\left(\frac{d\varphi}{d\tau}\right)^2$ are not forces because they are the part of the three-covariant derivative (as we know from the differential geometry course, the derivative in general case does not obey the tensor law transformation).

In the limit of $a\to 0$ the leading term $\Gamma^1_{00}\left(\frac{dt}{d\tau}\right)^2$ in the geodesic equation (2.4) becomes well-known Γ^1_{00} in the Schwarzschild spacetime $\Gamma^1_{00} = \frac{M}{r^2}\left(1-\frac{2M}{r}\right)$ which corresponds to the Newton force of the gravity attraction.

Comparing to the Schwarzschild case one can find that in the case of the equatorial plane $\theta=\pi/2$ the leading term Γ^1_{00Kerr} in the Kerr metric has the following connection to the leading term in Schwarzschild spacetime $\Gamma^1_{00\,sch}$.

$$\Gamma^1_{00Kerr} = \Gamma^1_{00\,sch} + \frac{a^2M}{r^4} \tag{2.5}$$

From this equation one can easily see that in the limit a→0 we have $\Gamma^1_{00Kerr} = \Gamma^1_{00\,sch}$ as we mentioned above. Also, one should notice that $\Gamma^1_{00Kerr} \geq \Gamma^1_{00\,sch}$. The term $2\Gamma^1_{03}\frac{dt}{d\tau}\frac{d\varphi}{d\tau} = 2\frac{-aM\Delta}{r^4}\frac{dt}{d\tau}\frac{d\varphi}{d\tau}$ corresponds to the Coriolis force. This type of force is absent in Schwarzschild spacetime because $\Gamma^1_{03} = 0$ if $a\to 0$ pends upon the angular momentum of the black hole.

The main goal of this paper is to find out which forces act on the particle with zero energy. To find the particle energy one should write down the Lagrangian in Kerr spacetime which has the following form:

$$L = \frac{1}{2}g_{ik}\frac{dx^i}{d\tau}\frac{dx^k}{d\tau} \tag{2.6}$$

From this Lagrangian (2.6) one can easily obtain the energy E and angular momentum L.

$$E = -\frac{dL}{d\dot{t}} = \left(1-\frac{2M}{\mathrm{r}}\right)\frac{dt}{d\tau} + \frac{2Ma}{\mathrm{r}}\frac{d\varphi}{d\tau} \tag{2.7}$$

$$L = \left(r^2 + a^2 + \frac{2Ma^2}{r}\right)\frac{d\varphi}{d\tau} + \frac{2Ma}{\mathrm{r}}\frac{dt}{d\tau} \tag{2.8}$$

From (2.8) one can easily see that the energy E might be either negative or equal to zero in the ergosphere of a rotating black hole (e. g., in the region $M+\sqrt{M^2-a^2} \leq r \leq 2M$).

 https://www.doi.org/10.33910/2687-153X-2021-2-4-180-184

Forces in the zero energy case

In the previous section we found out that the energy in the ergosphere of a rotating black hole might be either negative or equal to zero. In this section we will consider the forces which act on the particle with zero energy. For this purpose, let us find out how the radial geodesic depends upon an energy E. Substituting (2.7), (2.8) into (2.4), one obtains:

$$\begin{aligned}\frac{d^2r}{d\tau^2} &= -\frac{M\Delta}{r^4}\left(\frac{dt}{d\tau}\right)^2 + \frac{2aM\Delta}{r^4}\frac{dt}{d\tau}\frac{d\varphi}{d\tau} + \frac{Mr-a^2}{r\Delta}\left(\frac{dr}{d\tau}\right)^2 \\ &+ \frac{\Delta\left(2r-\frac{2a^2M}{r^2}\right)}{r^2}\left(\frac{d\varphi}{d\tau}\right)^2 = \\ &= -E\frac{M}{r^2}\frac{dt}{d\tau} - \frac{Ma^2}{r^4}\left(\frac{dt}{d\tau}\right)^2 + 2aM\left(\frac{r^2-Mr+a^2}{r^4}\right)\frac{dt}{d\tau}\frac{d\varphi}{d\tau} \\ &+ \frac{Mr-a^2}{r\Delta}\left(\frac{dr}{d\tau}\right)^2 + \frac{\Delta\left(2r-\frac{2a^2M}{r^2}\right)}{r^2}\left(\frac{d\varphi}{d\tau}\right)^2\end{aligned} \tag{3.1}$$

Now, if we put $E = 0$ in (3.1), we obtain the second order radial geodesic equation for the particle with zero energy:

$$\begin{aligned}\frac{d^2r}{d\tau^2} &= -\frac{Ma^2}{r^4}\left(\frac{dt}{d\tau}\right)^2 + 2aM\left(\frac{r^2-Mr+a^2}{r^4}\right)\frac{dt}{d\tau}\frac{d\varphi}{d\tau} + \frac{Mr-a^2}{r\Delta}\left(\frac{dr}{d\tau}\right)^2 \\ &+ \frac{\Delta\left(2r-\frac{2a^2M}{r^2}\right)}{r^2}\left(\frac{d\varphi}{d\tau}\right)^2\end{aligned} \tag{3.2}$$

As one can see, we have $\frac{Ma^2}{r^4}\left(\frac{dt}{d\tau}\right)^2$ from the leading term $\Gamma^1_{00}\left(\frac{dt}{d\tau}\right)^2$. This is the same term in which the Kerr leading term differs from the Schwarzschild one. One can notice that in the case of small rotation a^2M^2 the leading term is negligible. Thus, the analogue the Newtonian force of attraction is negligible for the particles with zero energy and small rotation. However, as one can see from Fig. 1, the leading term Γ^1_{00} if $E = 0$ is bigger than the one with positive energy.

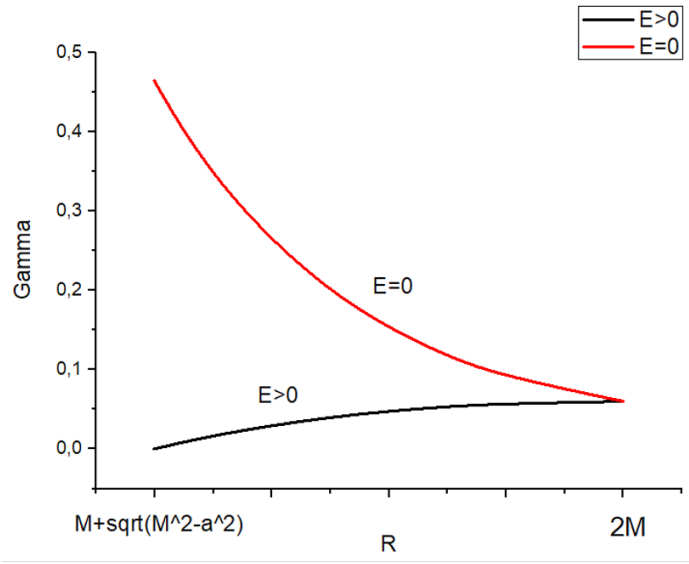

Fig. 1. Leading term

However, if we compare the Coriolis force for usual particle with positive energy and one with zero energy, we can see that for zero energy case the Coriolis force is bigger than in the case of the positive force (Fig. 2). We can state this because we have the main condition—the movement forward in time i. g. $\frac{dt}{d\tau}$ must be positive. This condition demands the positivity of $\frac{d\varphi}{d\tau}$.

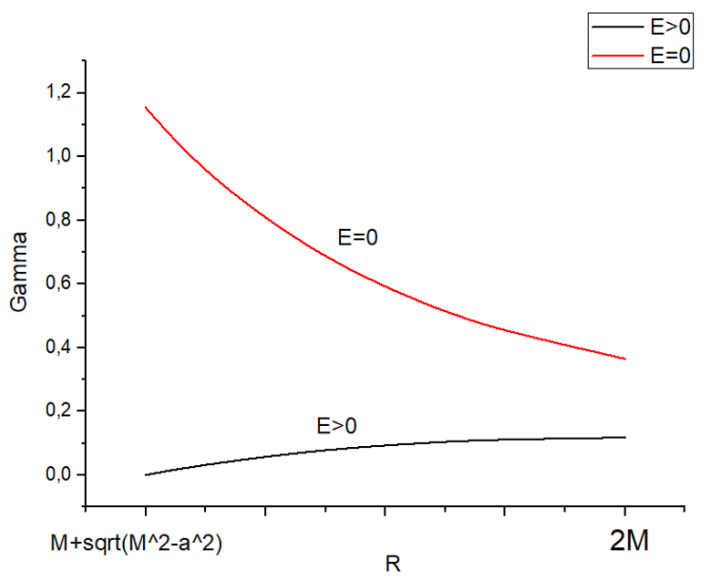

Fig. 2. Coriolis force

Conclusion

In this paper we have considered forces in the Kerr spacetime which act on the particles with zero energy. We showed that in the case of the leading term Γ^1_{00} of the radial geodesic equation, in the case of zero energy and of small rotation, nearly vanishes and we have the term which shows how the leading term in the Kerr metric differs from the one in Schwarzschild spacetime. It is worth noticing that this force component for particle with zero energy is bigger than the one with positive energy. Regarding the Coriolis force, the radial component of this force in the case of zero energy is bigger than the same component in the case of positive energy. The main result of this paper is that all force components for the particles with zero energy are bigger than the ones for particles with positive energy.

Conflict of Interest

The authors declare that there is no conflict of interest, either existing or potential.

Reference

Chandrasekhar, S. (1983) *The mathematical theory of black holes*. New York: Clarendon Press, 646 p. (In English)

Grib, A. A., Pavlov, Yu. V. (2017) Black holes and particles with zero or negative energy. *Theoretical and Mathematical Physics*, 190 (2), 268–278. https://doi.org/10.1134/S0040577917020088 (In English)

Grib, A. A., Pavlov, Yu. V., Vertogradov, V. D. (2014) Geodesics with negative energy in the ergosphere of rotating black holes. *Modern Physics Letters A*, 29 (20), 14501–14510. https://doi.org/10.1142/S0217732314501107 (In English)

Landau, L. D., Lifshitz, E. M. (1976) *Course of Theoretical Physics Series: In 10 vols. Vol. 2. The classical theory of fields*. 4th ed. Oxford: Butterworth-Heinemann Publ., 444 p. (In English)

Penrose, R. (2002) "Golden Oldie": Gravitational collapse: The role of general relativity. *General Relativity and Gravitation,* 34 (7), 1141–1165. https://doi.org/10.1023/A:1016578408204 (In English)

Poisson, E. (2004) *A relativist's toolkit: The mathematics of black-hole mechanics*. Cambridge: Cambridge University Press, 233 p. https://doi.org/10.1017/CBO9780511606601 (In English)

Teukolsky, S. A. (2015) The Kerr metric. *Classical and Quantum Gravity*, 32 (12), article 124006 https://doi.org/10.1088/0264-9381/32/12/124006 (In English)

Vertogradov, V. D. (2015) Geodesics for particles with negative energy in Kerr's metric. *Gravitation and Cosmology*, 21 (2), 171–174. https://www.doi.org/10.1134/S0202289315020115 (In English)

Vladimirov, Yu. S. (2009) *Klassicheskaya teoriya gravitatsii [Classical gravity theory]*. Moscow: Librokom Publ., 264 p. (In Russian)